

1 Heterogeneous Kinetics of H₂O, HNO₃ and HCl on HNO₃ 2 hydrates (α -NAT, β -NAT, NAD) in the range 175-200 K

3 R. Iannarelli^{1,2} and M. J. Rossi¹

4 ¹Laboratory of Atmospheric Chemistry (LAC), Paul Scherrer Institute (PSI), CH-5232 PSI
5 Villigen, Switzerland; ²New address: Safety, Prevention and Health Domain, RI DSPS-SCC ,
6 Station 6, Ecole Polytechnique Fédérale de Lausanne (EPFL), CH-1015 Ecublens,
7 Switzerland.

8 Correspondence to: M. J. Rossi (michel.rossi@psi.ch)

9

10 Abstract

11 Experiments on the title compounds have been performed using a multidagnostic stirred-flow
12 reactor (SFR) in which the gas- as well as the condensed phase has been simultaneously
13 investigated under stratospheric temperatures in the range 175-200 K. Wall interactions of the
14 title compounds have been taken into account using Langmuir adsorption isotherms in order
15 to close the mass balance between deposited and desorbed (recovered) compounds. Thin solid
16 films at 1 μ m typical thickness have been used as a proxy for atmospheric ice particles and
17 have been deposited on a Si window of the cryostat with the optical element being the only
18 cold point in the deposition chamber. FTIR absorption spectroscopy in transmission as well as
19 partial and total pressure measurement using residual gas MS and sensitive pressure gauges
20 have been employed in order to monitor growth and evaporation processes as a function of
21 temperature using both pulsed and continuous gas admission and monitoring under SFR
22 conditions. Thin solid H₂O ice films were used as the starting point throughout, with the
23 initial spontaneous formation of α -NAT followed by the gradual transformation of α - \rightarrow β -
24 NAT at T > 185 K. NAD was spontaneously formed at somewhat larger partial pressures of
25 HNO₃ deposited on pure H₂O ice. In contrast to published reports the formation of α -NAT
26 proceeded without prior formation of an amorphous HNO₃/H₂O layer and always resulted in
27 β -NAT. For α - and β -NAT the temperature dependent accommodation coefficient α (H₂O)
28 and α (HNO₃), the evaporation flux J_{ev}(H₂O) and J_{ev}(HNO₃) and the resulting saturation vapor
29 pressure P_{eq}(H₂O) and P_{eq}(HNO₃) were measured and compared to binary phase diagrams of
30 HNO₃/H₂O in order to afford thermochemical check of the kinetic parameters. The resulting

31 kinetic and thermodynamic parameters of activation energies for evaporation (E_{ev}) and
32 standard heats of evaporation ΔH_{ev}^0 of H_2O and HNO_3 for α - and β -NAT, respectively, led to
33 an estimate for the relative standard enthalpy difference between α - and β -NAT of -6.0 ± 20
34 kJ/mol in favor of β -NAT, as expected, despite a significantly larger value of E_{ev} for HNO_3 in
35 α -NAT. This in turn implies a substantial activation energy for HNO_3 accommodation in α -
36 compared to β -NAT where $E_{acc}(HNO_3)$ is essentially zero. The kinetic ($\alpha(HCl)$, $J_{ev}(HCl)$) and
37 thermodynamic ($P_{eq}(HCl)$) parameters of HCl-doped α - and β -NAT have been determined
38 under the assumption that HCl adsorption did not significantly affect $\alpha(H_2O)$ and $\alpha(HNO_3)$ as
39 well as the evaporation flux $J_{ev}(H_2O)$. $J_{ev}(HCl)$ and $P_{eq}(HCl)$ on both α - and β -NAT are larger
40 than the corresponding values for HNO_3 across the investigated temperature range but
41 significantly smaller than the values for pure H_2O ice at $T < 200$ K.

42

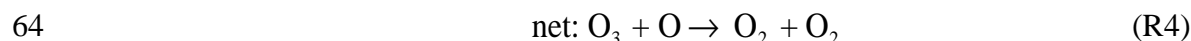
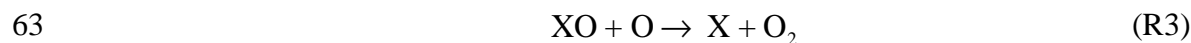
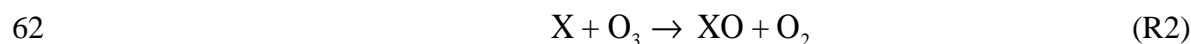
43 **1 Introduction**

44 Heterogeneous processes taking place on ice clouds in the Upper Troposphere (UT) or on
45 Polar Stratospheric Clouds (PSC's) in the Lower Stratosphere (LS) have, since a long time,
46 been recognized as one of the major ozone depleting mechanism (Solomon et al., 1986).
47 PSC's consist of either particles of crystalline nitric acid trihydrate (NAT) (type Ia), ternary
48 $H_2SO_4/HNO_3/H_2O$ supercooled solutions (type Ib) or pure H_2O ice (type II) (Zondlo et al.
49 2000) and are formed during the polar winter season when temperatures are sufficiently low
50 in order to allow H_2O supersaturation that ultimately leads to cloud formation in the dry
51 stratosphere subsequent to ice nucleation (Peter, 1997).

52 Ozone is depleted during the Arctic and Antarctic spring season after unreactive chlorine
53 reservoir compounds, $ClONO_2$ and HCl , are converted into molecular chlorine and rapidly
54 photolyze into active atomic chlorine during the spring season (Solomon, 1990). The presence
55 of PSC's enables heterogeneous chemical reactions such as Reaction (R1), which represents
56 one of the most efficient stratospheric heterogeneous reactions (Friedl et al, 1986; Molina et
57 al., 1985, 1987):



59 Reaction (R1) is orders of magnitude faster than the corresponding homogeneous gas phase
60 process (Molina et al., 1985) and the most important chlorine-activating reactions in the polar
61 stratosphere are reported in Reactions (R2)-(R4):



65 where X is H, OH, NO, Cl or Br leading to HO_x, NO_x, ClO_x and BrO_x catalytic cycles,
66 respectively.

67 Reaction (R1) increases the concentration of HNO₃ in the condensed phase and when PSC
68 particles become sufficiently large they fall out of the stratosphere (Fahey et al., 2001) which
69 inhibits Reaction (R5):



71 and prevents formation of reservoir species with longer atmospheric residence times.

72 The study of HNO₃ interaction with ice in the temperature and pressure ranges typical of the
73 UT/LS is crucial in order to understand the de-nitrification process initiated by reaction (R1)
74 and its effectiveness in the overall ozone destruction mechanism. To this purpose, many
75 research groups (Voigt et al., 2000, 2005; Fahey et al., 2001; Schreiner et al., 2003; Gao et al.,
76 2004; Höpfner et al., 2006) have studied the composition of PSC's using both *in situ* and
77 remote sensing techniques both in the Arctic as well as above Antarctica. A balloon borne
78 experiment at first detected non-crystalline HNO₃ hydrates (Schreiner et al., 1999), later both
79 balloon borne (Voigt et al., 2000; Schreiner et al., 2003) and aircraft campaigns (Voigt et al.,
80 2005) obtained unambiguous proof of the presence of crystalline HNO₃ hydrates (NAT) at
81 altitudes between 18 and 24 km in the Arctic. The presence of β-NAT, through the
82 identification of type Ia PSC's, has been unambiguously confirmed by Höpfner et al. (2006)
83 using the MIPAS instrument on a satellite platform by comparison of measured limb-emission
84 spectra of polar stratospheric clouds with measured optical constants in the region of the
85 symmetric NO₃ peak at $\nu_2 = 820 \text{ cm}^{-1}$.

86 The existence of several crystalline hydrates of nitric acid has been confirmed for several
87 years. Hanson and Mauersberger (1988) have identified two stable hydrates, namely, nitric
88 acid monohydrate (NAM, HNO₃•H₂O) and nitric acid trihydrate (NAT, HNO₃•3H₂O) the
89 latter of which is thought to be of atmospheric importance. Several distinct crystalline
90 hydrates of HNO₃ have been found by Ritzhaupt and Devlin (1991) in their work examining
91 the infrared absorption spectrum of thin film samples. By depositing the equilibrium vapours

92 of aqueous HNO_3 solutions of different concentrations at 293 K they observed nitric acid
93 dihydrate (NAD, $\text{HNO}_3 \cdot 2\text{H}_2\text{O}$), NAM and NAT. Ji and Petit have performed an extensive
94 investigation on the thermochemical properties of NAD (Ji and Petit, 1993).

95 Tolbert and coworkers have also reported infrared absorption spectra of NAM, NAD and
96 NAT in a series of studies. Tolbert and Middlebrook (1990) have co-condensed calibrated
97 mixtures of $\text{H}_2\text{O}/\text{HNO}_3$ vapours onto a cryostat and assigned the absorption spectra of the
98 growing thin films to nitric acid hydrates (NAM, NAD or NAT) according to the ratio of the
99 dosing gases. Koehler et al. (1992) have observed the Fourier transform infrared (FTIR)
100 absorption spectra in transmission of nitric acid hydrate thin films and measured their
101 composition using temperature-programmed desorption (TPD). They confirmed the
102 previously assigned spectra of NAD and NAM. They were also the first to observe two
103 distinct structures of NAT: a low-temperature and metastable structure called α -NAT whose
104 structure has recently been elucidated (Weiss et al., 2016) and a thermodynamically stable
105 high-temperature structure named β -NAT. Middlebrook et al. (1992) observed that NAD
106 consistently converts to β -NAT when exposed to H_2O partial pressures typical of the
107 stratosphere and therefore proposed that NAD is also metastable under stratospheric
108 conditions.

109 Several other groups have investigated the structure of nitric acid hydrates and published
110 absorption spectra of both α -NAT and β -NAT in the mid-IR range, using grazing incidence
111 Reflection Absorption IR spectroscopy (RAIRS) (Zondlo et al., 1998; Zondlo et al., 2000;
112 Ortega et al., 2003; Ortega et al., 2006; Herrero et al., 2006; Escribano et al., 2007) and FTIR
113 in transmission (Tso and Leu, 1996; Martin-Llorente et al., 2006; Ortega et al., 2006).

114 Compared to the molecular properties of the nitric acid hydrates knowledge of the kinetic
115 parameters of trace gases interacting with HNO_3 hydrates is scarce. Middlebrook et al. (1992)
116 have used time-dependent FTIR monitoring of the optical density of growing NAT films
117 during deposition to measure the uptake of H_2O and HNO_3 on NAT. They reported a value of
118 $\gamma_{\text{NAT}}(\text{HNO}_3) > 0.4$ for HNO_3 net uptake (γ) on NAT at $T = 197$ K whereas $2.0 \times 10^{-3} \leq$
119 $\gamma_{\text{NAT}}(\text{H}_2\text{O}) \leq 1.0 \times 10^{-2}$ is reported for H_2O . The range measured for $\gamma_{\text{NAT}}(\text{H}_2\text{O})$ corresponds to
120 the HNO_3 pressure used during the deposition. Using evaporation experiments in a slow-flow
121 reactor Biermann et al. (1998) measured the accommodation coefficient of H_2O on β -NAT
122 substrates, $\alpha_{\beta\text{-NAT}}(\text{H}_2\text{O})$, from the thickness of the substrate measured using FTIR

123 absorption. They found no temperature dependence, reporting lower limiting values of
124 $\alpha_{\beta\text{-NAT}}(\text{H}_2\text{O}) = (2.2 - 6.0) \times 10^{-2}$ in the range 192-202 K.

125 Delval and Rossi (2005) have used a multidiagnostic flow reactor, similar to the one used in
126 this work, coupled with a quartz crystal microbalance (QCMB) for the measurement of the
127 evaporation rate of H_2O from $\alpha\text{-NAT}$ and $\beta\text{-NAT}$ thin films. They reported a positive
128 temperature dependence of $\alpha_{\alpha\text{-NAT}}(\text{H}_2\text{O})$ and a negative temperature dependence of
129 $\alpha_{\beta\text{-NAT}}(\text{H}_2\text{O})$ in the range 179-208 K.

130 Hanson (1992) also measured the uptake coefficient of HNO_3 on NAT using a cold coated-
131 wall flow tube with HNO_3 deposited on ice condensed on the cold flow tube walls and
132 reported $\gamma_{\text{NAT}}(\text{HNO}_3) > 0.3$. A rapid uptake was observed which decreased as the surface
133 coverage or dose of HNO_3 increased. Furthermore, the observed steady state partial pressure
134 of HNO_3 over the ice substrate is about a factor of 5 higher than the HNO_3 vapor pressure
135 over NAT and thus indicates that no hydrate was actually formed during the experiments.
136 Therefore, the observed uptake has most likely to be attributed to uptake on other cold
137 surfaces in the flow reactor.

138 Reinhardt et al. (2003) reported $\gamma_{\text{NAT}}(\text{HNO}_3) = 0.165$ in the temperature range 160 to 170 K.
139 They used a slow flow reaction cell coupled with DRIFTS (Diffuse Reflectance Infrared
140 Fourier Transform Spectroscopy) for the detection of adsorbed species and downstream FTIR
141 for the detection of gas phase HNO_3 .

142 In the investigation of the properties of binary chemical systems the behavior of the simple
143 single-component systems is an important stepping stone. Hynes et al. (2002) observed
144 continuous uptake of HNO_3 on water-ice films below 215 K and time dependent uptake above
145 215 K, with the maximum uptake $\gamma_{\text{ice}}(\text{HNO}_3)$ decreasing from 0.03 at 215 K down to 0.006 at
146 235 K. They also observed that the uptake of HCl at 218 K on ice surfaces previously dosed
147 with HNO_3 is reversible. Furthermore, the adsorption of HNO_3 on ice surfaces which
148 contained previously adsorbed HCl indicates that HCl is displaced from surface sites by
149 HNO_3 .

150 In this work, the results for the kinetics of H_2O and HNO_3 gas interacting with
151 spectroscopically characterized HNO_3 hydrates will be presented. The independent
152 measurement of the absolute rate of evaporation R_{ev} [$\text{molec s}^{-1} \text{cm}^{-3}$] and the accommodation
153 coefficient α of H_2O and HNO_3 on $\alpha\text{-}$ and $\beta\text{-NAT}$ substrates is performed using a

154 combination of steady state and real-time pulsed valve experiments. Results on the kinetics of
155 the ternary system HCl on HNO₃ hydrates will also be presented. All experiments reported in
156 this work have been performed using a multidagnostic stirred flow reactor (SFR) in the
157 molecular flow regime, which has been described in detail before (Chiesa and Rossi, 2013;
158 Iannarelli and Rossi, 2014). In addition, all experiments have been performed under strict
159 mass balance control by considering how many molecules of HNO₃, HCl and H₂O were
160 present in the gas vs. the condensed phase (including the vessel walls) at any given time.
161 These experiments have been described by Iannarelli and Rossi (2015). Most importantly, the
162 consistency of the accommodation and evaporation kinetics has been checked using the
163 method of thermochemical kinetics (Benson, 1976) by calculating the equilibrium vapor
164 pressure and comparing it with values of published phase diagrams. In addition, the present
165 work is the first to present absolute rates of evaporation of all involved constituents (H₂O,
166 HNO₃, HCl) thus enabling predictions on evaporative lifetimes of ice particles under
167 atmospheric conditions.

168

169 **2 Experimental Apparatus and Methodology**

170 **2.1 Experimental Apparatus and Growth Protocols**

171 Figure 1 shows a diagram of the reactor used in this work with the experimental diagnostic
172 tools and Table 1 reports its characteristic parameters. Briefly, it consists of a low-pressure
173 stainless steel reactor, which may be used under static (all valves closed) or stirred flow (gate
174 valve closed, leak valves open) conditions. We use absolute total pressure measurement and
175 calibrated residual gas mass spectrometry (MS) to monitor the gas phase and FTIR
176 spectroscopy in transmission for the condensed phase. Thin solid films of up to 2 μm
177 thickness are grown on a temperature controlled Si substrate and an average of 8 scans are
178 recorded at 4 cm⁻¹ resolution in the spectral range 700-4000 cm⁻¹ at typical total scan time of
179 45-60 s.

180 The 1" Si window is the only cold spot in the reactor exposed to admitted gases and therefore
181 the only place where gas condensation occurs. This allows the establishment of a 1:1
182 correspondence between the thin film composition and the changes in the gas partial pressures
183 in the reactor. Experimental proof of mass balance has previously been reported for this setup
184 (Delval et al., 2003; Chiesa and Rossi, 2013; Iannarelli and Rossi, 2014; 2015).

185 The introduction of HNO₃ in the system forced us to slightly modify the inlet system used
186 previously (Iannarelli and Rossi, 2014) in order to take into account the fact that HNO₃ is an
187 extremely “sticky” molecule that interacts with the internal surfaces of the reservoir vessel of
188 the inlet system as well as with the reactor walls of the SFR (Iannarelli and Rossi, 2015). We
189 therefore minimized the volume of the admission system and only retained the absolutely
190 necessary total pressure gauge for measuring the absolute inlet flow rate (molecule s⁻¹).

191 Similarly to the case of HCl and H₂O (Iannarelli and Rossi, 2014) we have described the
192 HNO₃ interaction with the reactor walls using a Langmuir adsorption isotherm and
193 determined the concentration of HNO₃ in the ice sample after calibration of HNO₃ following
194 the methodology described in Iannarelli and Rossi (2015). Table 2 reports the values of the fit
195 parameters of the Langmuir adsorption isotherms for all the gases interacting with the
196 stainless steel (SS304) internal surfaces of the SFR. Binary combinations of HNO₃/H₂O and
197 HCl/H₂O have been used to describe the interaction of the acidic probe gas with the vessel
198 walls in the presence of H₂O vapor.

199 The protocol for the growth of α-NAT, β-NAT and NAD thin films has also been described
200 in Iannarelli and Rossi (2015). Briefly, the protocol for either hydrate always starts with the
201 growth of pure ice: the chamber is backfilled under SFR conditions with water vapor at flow
202 rates between 5×10¹⁵ and 10¹⁶ molec s⁻¹, corresponding to a partial pressure of H₂O, p(H₂O)
203 between 4.7 and 9.4×10⁻⁴ Torr (both apertures open), with the Si substrate held at temperature
204 in the range 167 to 175 K. The pure ice film grows on both sides of the Si substrate to a
205 thickness of typically 1 μm until the H₂O flow is halted (Iannarelli and Rossi, 2014). The
206 temperature of the support is then set to the value used for the growth of the desired HNO₃
207 hydrate at a typical rate of ±0.3 K min⁻¹.

208 The growth protocols for α-NAT and NAD are similar and start after the deposition of a pure
209 ice film: the temperature of the Si substrate is held in the range 180 to 185 K for α-NAT and
210 at 168 K for NAD. The sample is exposed for approximately 10 min at SFR conditions to
211 HNO₃ vapor at flow rates in the range 3 to 7×10¹⁴ molecule s⁻¹ for α-NAT and 9×10¹⁴
212 molecule s⁻¹ for NAD. The typical total dose of HNO₃ admitted into the reactor is 2 to 3×10¹⁷
213 molecules and 4×10¹⁷ molecules for α-NAT and NAD, respectively, with almost all of it
214 adsorbed onto the ice film. In both cases, we observe the formation of a new phase after
215 approximately 5 min of exposure as shown in the change of the FTIR absorption spectrum.
216 The present experimental conditions seem to show that no nucleation barrier is present for α-

217 NAT and NAD growth, in agreement with previous works (Hanson, 1992; Middlebrook et al.,
218 1992; Biermann et al., 1998). In contrast, Zondlo et al. (2000) have shown that crystalline
219 growth occurs via an intermediate stage of supercooled H₂O/HNO₃ liquid forming over ice.
220 After exposure the temperature of the substrate is set to the desired value for the kinetic
221 experiments on α -NAT or NAD as a substrate.

222 The protocol for the growth of β -NAT is different compared to NAD and α -NAT hydrates as
223 it only starts after the growth of an α -NAT film. After the HNO₃ flow has been halted, the α -
224 NAT/ice system is set to static conditions and the temperature increased to 195 K. During the
225 temperature increase the α -NAT film converts to β -NAT as shown by means of FTIR
226 spectroscopy (Koehler et al., 1992; Iannarelli and Rossi, 2015), and once the conversion is
227 completed the temperature is set to the desired value to start the kinetic experiments using β -
228 NAT as substrate. Typical growth protocols under mass balance control showing both the
229 FTIR transmission as well as the corresponding MS signals of HNO₃ as a function of
230 deposition time have been published previously (Iannarelli and Rossi, 2015).

231 In all samples used for this work, we never have a pure HNO₃ hydrate because we always
232 operate under conditions of excess or comparable amounts of pure ice. Excess ice has been
233 shown to have a stabilizing effect on both α -NAT and β -NAT (Weiss et al., 2016) and in all
234 our experiments the presence of excess ice has been confirmed by FTIR spectra (Iannarelli
235 and Rossi, 2015).

236 2.2 Experimental Methodology

237 The experimental methodology used in this work is an extension of the methodology reported
238 in Iannarelli and Rossi (2014) where the combination of real-time pulsed valve and steady
239 state experiments allowed the independent measurement of the rate of evaporation R_{ev} [molec
240 s⁻¹ cm⁻³] and the accommodation coefficient α of HCl and H₂O on crystalline and amorphous
241 HCl hydrates.

242 For each gas X (X = H₂O, HNO₃, HCl) admitted into the reactor in the presence of ice, the
243 following flow balance equation holds at steady state:

$$244 \quad F_{in}(X) + F_{des}(X) + F_{ev}(X) = F_{SS}(X) + F_{ads,w}(X) + F_{ads,ice}(X) \quad (1)$$

245 All terms in Equation (1) are flow rates in molec s⁻¹ with the terms from left to right
246 corresponding to molecules admitted into the reactor (F_{in}), molecules desorbing from the

247 reactor walls (F_{des}), molecules evaporating from the ice surface (F_{ev}), molecules effusing
 248 through the leak valve into the MS chamber (F_{SS}), molecules adsorbing onto the reactor walls
 249 ($F_{ads,w}$) and molecules adsorbing onto the ice film ($F_{ads,ice}$).

250 Under the assumption that the adsorption onto the walls may be described as a Langmuir-type
 251 adsorption, Eq. (1) may be expressed as follows for a gas X:

$$\begin{aligned}
 & V \cdot R_{in}(X) + N_{TOT} \cdot k_{des,w}(X) \cdot \theta + V \cdot R_{ev}(X) = \\
 252 \quad & = V \cdot R_{SS}(X) + S_w \cdot \frac{\alpha_w(X) \cdot \bar{c}}{4} (1 - \theta) [X]_{SS} + S_{film} \cdot \frac{\alpha_{film}(X) \cdot \bar{c}}{4} [X]_{SS} \quad (2)
 \end{aligned}$$

253 where V is the reactor volume in cm^3 , $R_{in}(X)$ the rate of molecules X admitted into the
 254 chamber in $\text{molec} \cdot \text{s}^{-1} \cdot \text{cm}^{-3}$, N_{TOT} the total number of molecules X adsorbed on the reactor
 255 walls, $k_{des,w}(X)$ the desorption rate constant from the reactor walls in s^{-1} , θ the fractional
 256 surface coverage in terms of a molecular monolayer, $R_{ev}(X)$ the rate of evaporation of X from
 257 the ice in $\text{molec} \cdot \text{s}^{-1} \cdot \text{cm}^{-3}$, $R_{SS}(X)$ the rate of effusion through the leak valve in $\text{molec} \cdot \text{s}^{-1} \cdot \text{cm}^{-3}$,
 258 S_w and S_{film} the surfaces of the reactor walls and the thin film in cm^2 , $\alpha_w(X)$ and $\alpha_{film}(X)$ the
 259 accommodation coefficients of X on the walls and on the thin film, $[X]_{SS}$ the concentration at
 260 steady state in $\text{molec} \cdot \text{cm}^{-3}$ and \bar{c} the mean thermal velocity of a molecule in $\text{cm} \cdot \text{s}^{-1}$,
 261 respectively. The mathematical derivation of Eq. (2) may be found in Supplement B of
 262 Iannarelli and Rossi (2014).

263 Pulsed valve (PV) experiments and Langmuir adsorption isotherms have been used in order to
 264 measure $k_{des,w}(X)$ and $\alpha_w(X)$ (Iannarelli and Rossi, 2014), leaving only two unknown
 265 parameters in Eq. (2): $R_{ev}(X)$ and $\alpha_{film}(X)$. The Langmuir adsorption isotherms are shown in
 266 Figure S1 of Supplement A whereas the parameters for the best fit are reported in Table 2.

267 In the case of H_2O , once the selected substrate has been grown according to the protocol
 268 briefly described above, the film is set to a chosen temperature. After steady state conditions
 269 are established, a series of H_2O pulses are admitted into the reactor. The exponential decay of
 270 the MS signal at m/z 18 (k_d) is given by the sum of the measured k_{esc} , the adsorption rate
 271 constant on the walls (k_w) and the adsorption rate constant (k_c) onto the ice, namely $k_d = k_{esc} +$
 272 $k_w + k_c$, in the aftermath of a pulse. The accommodation coefficient $\alpha_{film}(\text{H}_2\text{O})$ may then be
 273 calculated according to Eq. (3):

$$274 \quad \alpha_{film}(\text{H}_2\text{O}) = \frac{k_c(\text{H}_2\text{O})}{\omega(\text{H}_2\text{O})} \quad (3)$$

275 where $\omega(\text{H}_2\text{O})$ is the calculated gas-surface collision frequency in s^{-1} and is reported in Table
276 1.

277 The steady state MS signal established before the pulse series represents the calibrated flow
278 rate of molecules effusing through the leak valve, $F_{\text{SS}}(\text{H}_2\text{O})$, in Eq. (1) and may be used to
279 calculate the concentration at steady state $[\text{X}]_{\text{SS}}$ according to Eq. (4):

$$280 \quad [\text{X}]_{\text{SS}} = \frac{F_{\text{SS}}(\text{X})}{k_{\text{esc}}(\text{X})V} \quad (4)$$

281 where $k_{\text{esc}}(\text{X})$ is the effusion rate constant of gas X out of the reactor in s^{-1} (see Table 1).
282 Finally, $[\text{X}]_{\text{SS}}$ is used to calculate $R_{\text{ev}}(\text{X})$ using Eq. (2).

283 Subsequently, the film is set to a higher temperature, $F_{\text{SS}}(\text{H}_2\text{O})$ is recorded and a series of H_2O
284 pulses applied to the same ice sample. This experimental protocol has been repeated for each
285 measured point in the temperature interval of interest.

286 Under the present experimental conditions, PV experiments of HNO_3 leading to transient
287 supersaturation of HNO_3 are hampered by excessive pulse broadening, most probably owing
288 to the strong adsorption of HNO_3 on ice and the stainless steel vessel walls that makes the
289 observation and interpretation of a HNO_3 pulse difficult for low doses in the presence of ice.
290 In this case the advantage of the PV technique as a real-time method of observation is lost.

291 Therefore, in order to measure the kinetics of HNO_3 gas in the presence of α -NAT, β -NAT
292 and NAD ice films we have used the two-orifice method first described by Pratte et al. (2006).
293 It has been modified to take into account the interaction of HNO_3 with the internal walls of
294 the SFR. The two-orifice method has also been used to measure the kinetics of H_2O on HNO_3
295 hydrates in order to compare these results with the results of PV experiments for H_2O .

296 The two-orifice (TO) method allows the separation of the rate of evaporation $R_{\text{ev}}(\text{X})$ and the
297 condensation rate constant $k_{\text{c}}(\text{X})$ of a gas X by choosing two different escape orifices and
298 measuring the corresponding value of concentration $[\text{X}]_{\text{SS}}$ at steady state of gas X inside the
299 reactor. By alternatively opening the small orifice (S) and both orifices (M) (see Figure 1),
300 two steady state equations hold for a probe gas X which are reported in Eqs. (5) and (6) taking
301 into account the interaction with the reactor walls:

$$302 \quad R_{\text{ev}}(\text{X}) + \frac{N_{\text{TOT}}}{V} \cdot k_{\text{des,w}}(\text{X}) \cdot \theta = (k_{\text{c}}(\text{X}) + k_{\text{esc}}^{\text{S}}(\text{X})) \cdot [\text{X}]_{\text{SS}}^{\text{S}} + \frac{k_{\text{w}}(\text{X})}{V} \cdot (1 - \theta) \cdot [\text{X}]_{\text{SS}}^{\text{S}}$$

303 (5)

$$R_{ev}(X) + \frac{N_{TOT}}{V} \cdot k_{des,w}(X) \cdot \theta = (k_c(X) + k_{esc}^M(X)) \cdot [X]_{SS}^M + \frac{k_w(X)}{V} \cdot (1 - \theta) \cdot [X]_{SS}^M \quad (6)$$

where the superscripts indicate small orifice only (S) or both orifices (M) open, respectively.

The kinetic parameters $R_{ev}(X)$ and $k_c(X)$ are calculated from Eqs. (7) and (8) as follows:

$$k_c(X) = \frac{k_{esc}^M(X) \cdot [X]_{SS}^M - k_{esc}^S(X) \cdot [X]_{SS}^S}{[X]_{SS}^S - [X]_{SS}^M} - k_w(X) \cdot (1 - \theta) \quad (7)$$

$$R_{ev}(X) = \frac{(k_{esc}^M(X) - k_{esc}^S(X)) \cdot [X]_{SS}^S \cdot [X]_{SS}^M}{[X]_{SS}^S - [X]_{SS}^M} - \frac{N_{TOT}}{V} \cdot k_{des,w}(X) \cdot \theta \quad (8)$$

This method leads to larger uncertainties for both $R_{ev}(X)$ and $k_c(X)$ compared to the combined PV and steady state method used before. The reason lies in the fact that two similarly large numbers, namely $[X]_{SS}^S$ and $[X]_{SS}^M$, are subtracted in the denominators of equations Eqs. (7) and (8) leading to a small and therefore uncertain value of $k_c(X)$ and $R_{ev}(X)$. In other words, the noise in the signal from the MS is such that the two data sets for the small orifice and both orifices open are sometimes insufficiently linearly independent of each other within experimental uncertainty.

We also used the combination of real-time PV and steady state experiments using HCl as a probe gas and applied the experimental method described previously in order to measure the kinetics of HCl, $R_{ev}(HCl)$ and $\alpha(HCl)$, in the presence of α -NAT and β -NAT ice films.

Once the kinetics $R_{ev}(X)$ and $k_c(X)$ have been measured using the combination of PV and steady state experiments (H_2O , HCl) or the two-orifice method (HNO_3 , H_2O), we may calculate the equilibrium vapor pressure $P_{eq}(X)$ for each gas according to Eq. (9):

$$P_{eq}(X) = \frac{R_{ev}(X)}{k_c(X)} \cdot \frac{RT}{N_A} \quad (9)$$

where R is the molar gas constant in $cm^3 \text{ Torr K}^{-1} \text{ mol}^{-1}$, T the temperature of the thin film in K and N_A Avogadro's constant in molec mol^{-1} .

3 Results

3.1 Crystalline α -NAT Thin Films

The kinetic results for the heterogeneous interaction of H_2O and HNO_3 with α -NAT and NAD thin films obtained in PV and TO experiments are displayed in Figure 2. Full symbols represent PV experiments: full red circles correspond to experiments on α -NAT substrates,

331 and full green squares to experiments on NAD substrates. Empty symbols represent TO
332 experiments with red circles representing H₂O and black triangles HNO₃ results. Pure ice
333 experiments are displayed as inverse blue triangles for comparison purposes. The calculated
334 relative error for PV experiments is 30% whereas for TO experiments we estimate a relative
335 error of 60%. We refrain at this point from showing raw data (FTIR absorption spectra and
336 MS data as a function of time) because representative samples have been shown by Iannarelli
337 and Rossi (2015) for α - and β -NAT. We will defer the presentation of raw data on the
338 interaction of HCl on α - and β -NAT to Section 3.3 below.

339 Figure 2a shows the measured accommodation coefficients $\alpha_{\alpha\text{-NAT}}(\text{X})$, ($\text{X} = \text{H}_2\text{O}, \text{HNO}_3$), as
340 a function of temperature. $\alpha_{\alpha\text{-NAT}}(\text{H}_2\text{O})$ in PV experiments (full red circles) decreases as a
341 function of temperature in the range 167-188.5 K, varying from 0.08 at 167 K to 3.1×10^{-3} at
342 188.5 K, which is a factor of 30 lower than $\alpha_{\text{ice}}(\text{H}_2\text{O})$ on pure ice at the same temperature.
343 The scatter in the data is not an artifact and is due to the sample-to-sample variability of the
344 crystalline samples we use and the randomness of the crystalline nucleation process. The
345 variability may be in surface composition, morphology and smoothness as shown in previous
346 studies (McNeill et al., 2007; Iannarelli and Rossi, 2014).

347 $\alpha_{\alpha\text{-NAT}}(\text{H}_2\text{O})$ in TO experiments (empty red circles) yields different results. For temperatures
348 lower than 185 K it is equal to $\alpha_{\alpha\text{-NAT}}(\text{H}_2\text{O})$ on α -NAT in PV experiments within
349 experimental error. For temperatures higher than 185 K $\alpha_{\alpha\text{-NAT}}(\text{H}_2\text{O})$ increases as a function
350 of temperature in contrast to results of PV experiments (full red circles) varying from 8×10^{-3}
351 at 183 K to 0.08 at 193.5 K, being equal to $\alpha_{\text{ice}}(\text{H}_2\text{O})$ on pure ice within experimental error at
352 the highest temperature. This result compares favorably with the results of Delval and Rossi
353 (2005) which showed a positive temperature dependence of $\alpha_{\alpha\text{-NAT}}(\text{H}_2\text{O})$ in the temperature
354 range 182-207 K. $\alpha_{\text{NAD}}(\text{H}_2\text{O})$ in PV experiments (full green squares) is equal within
355 experimental error to $\alpha_{\alpha\text{-NAT}}(\text{H}_2\text{O})$.

356 $\alpha_{\alpha\text{-NAT}}(\text{HNO}_3)$ (black empty triangles) increases as a function of temperature in the measured
357 temperature range from a value of approximately 0.005 at 181 K to a value of 0.13 at 188 K.
358 The narrow temperature range follows from the high uncertainties of the two-orifice method
359 at low temperatures and the increasingly rapid conversion of α -NAT to β -NAT at high
360 temperatures. These values are lower by a factor of 2 to 40 compared to the preferred values
361 indicated by the IUPAC Subcommittee on Gas Kinetic Data Evaluation (Crowley et al.,
362 2010).

363 Figure 2b shows results for the rate of evaporation $R_{ev}(X)$ in $\text{molec s}^{-1} \text{cm}^{-3}$ as a function of
364 temperature. The same symbols as for panel (a) are used. $R_{ev}(\text{H}_2\text{O})$ on α -NAT in PV
365 experiments is lower by a factor of 2 compared to $R_{ev}(\text{H}_2\text{O})$ on pure ice at temperatures lower
366 than 175 K. For temperatures higher than 175 K, $R_{ev}(\text{H}_2\text{O})$ on α -NAT is lower on average by
367 up to a factor of 50 compared to $R_{ev}(\text{H}_2\text{O})$ on pure ice. This result is very different compared
368 to the previously studied case of the binary system HCl amorphous and crystalline
369 hexahydrate using the same apparatus (Iannarelli and Rossi, 2013), where the evaporation of
370 H_2O takes place at a rate characteristic of pure ice despite the presence of adsorbed HCl on
371 the ice and is in agreement with the findings of Delval and Rossi (2005).

372 $R_{ev}(\text{H}_2\text{O})$ on α -NAT measured using the TO method is equal within experimental error to
373 $R_{ev}(\text{H}_2\text{O})$ obtained in PV experiments. $R_{ev}(\text{H}_2\text{O})$ on NAD is equal to within experimental
374 error to $R_{ev}(\text{H}_2\text{O})$ on α -NAT. The full black line shows the rate of evaporation of pure water
375 for the system in use, calculated from literature results of the equilibrium vapor pressure
376 (Marti and Mauersberger, 1993) using $\alpha = 1$, whereas the dashed black line represents
377 extrapolated values of $R_{ev}(\text{H}_2\text{O})$ for temperatures lower than 173 K using the expression
378 provided by Mauersberger and coworkers (Marti and Mauersberger, 1993; Mauersberger and
379 Krankowsky, 2003).

380 Figure 2c shows the results for $P_{eq}(X)$ in Torr calculated according to Eq. (9) for both H_2O
381 and HNO_3 as a function of temperature. The same symbols as in panels (a) and (b) are used.
382 $P_{eq}(\text{H}_2\text{O})$ of α -NAT calculated from the kinetic parameters measured in PV experiments is
383 lower by a factor of approximately 3 compared to $P_{eq}(\text{H}_2\text{O})$ on pure ice at temperatures higher
384 than 180 K. For temperatures lower than 180 K $P_{eq}(\text{H}_2\text{O})$ of α -NAT is close to $P_{eq}(\text{H}_2\text{O})$ of
385 pure ice because the present samples are water-rich (Molina, 1994) with a HNO_3 mole
386 fraction of less than 10%.

387 $P_{eq}(\text{H}_2\text{O})$ of α -NAT calculated from the results of TO experiments is lower by up to a factor
388 of 10 compared to $P_{eq}(\text{H}_2\text{O})$ of pure ice in the temperature range 180-193.5 K. At
389 temperatures lower than 180 K, $P_{eq}(\text{H}_2\text{O})$ of α -NAT from TO experiments is equal within
390 experimental error to $P_{eq}(\text{H}_2\text{O})$ of α -NAT in PV experiments. $P_{eq}(\text{HNO}_3)$ of α -NAT is lower
391 by a factor of 1000 in the temperature range 181-188 K compared to $P_{eq}(\text{H}_2\text{O})$ on pure ice.

392 The values obtained for the equilibrium vapor pressure have been compared with the
393 $\text{HNO}_3/\text{H}_2\text{O}$ phase diagram constructed by McElroy et al. (1986); Hamill et al. (1988); Molina
394 (1994). Figure 3 shows the results for α -NAT and metastable NAD films, PV and TO

395 experiments. The solid lines represent the coexistence conditions for two phases and the
396 dashed lines represent vapor pressures of liquids with composition given as % (w/w) of
397 HNO₃. The shaded rectangular area represents typical polar stratospheric conditions. The
398 slope *m* of the coexistence lines depends on the difference of the enthalpies of sublimation of
399 the two acid hydrate species, namely NAM and NAT, according to Eq. (10) (Wooldridge et
400 al., 1995):

$$401 \quad m = \frac{\Delta H_{\text{subl}}^1 - \Delta H_{\text{subl}}^2}{(n_1 - n_2) R} \quad (10)$$

402 where ΔH_{subl}^1 and ΔH_{subl}^2 are the enthalpies of sublimation of the acid hydrates in kJ/mol, n_1
403 and n_2 the number of water molecules of the respective hydrate and *R* is the gas constant in J
404 mol⁻¹ K⁻¹. The slope of the ice/NAT coexistence line is calculated from Wooldridge et al.
405 (1995) as $m_{\text{ice/NAT}} = (50.9 \text{ kJ/mol})/R$ and for NAT/NAM $m_{\text{NAT/NAM}} = (55.9 \text{ kJ/mol})/R$.

406 All α -NAT experiments lie in the existence area of nitric acid trihydrate, as expected. On the
407 other hand, α -NAT under polar stratospheric conditions (shaded rectangular area) is unstable
408 and starts to convert into the stable β -NAT phase (Koehler et al., 1992). The small number of
409 α -NAT samples we reported in the shaded gray area is further confirmation of results reported
410 in the literature because lower temperatures are needed to slow down the conversion of α to
411 β -NAT. NAD samples are expected to lie closer to the monohydrate region, given their
412 composition close to the H₂O:HNO₃ = 2:1 stoichiometry (Iannarelli and Rossi, 2015).
413 Nevertheless, the pure ice phase is still dominant in the present samples and all samples are
414 water-rich (Molina, 1994) with a HNO₃ mole fraction of less than 10% even in NAD films.

415 **3.2 Crystalline β -NAT Thin Films**

416 The results for β -NAT thin films obtained in PV and TO experiments are displayed in Figure
417 4. Full and empty red squares represent PV and TO experiments, respectively, with red
418 squares representing H₂O and black triangles HNO₃ results. Pure ice experiments are
419 displayed as inverse blue triangles for comparison.

420 The largest uncertainty in our experiment is that of the flow rate introduced into the reactor,
421 which is assigned a relative error of 25%. The flow rate measurement affects the calibration
422 of the MS and therefore the measurement of all the concentrations in the reactor (Eq. 4).
423 Therefore, we estimate a global relative error of 30% for PV experiments and double this

424 uncertainty for TO experiments because Equations (7) and (8) imply a difference of two large
425 numbers in many cases, as discussed above. We therefore assign a global 60% relative error
426 to results obtained in TO experiments.

427 Figure 4a shows the measured $\alpha_{\beta\text{-NAT}}(X)$ as a function of temperature: $\alpha_{\beta\text{-NAT}}(\text{H}_2\text{O})$
428 resulting from PV experiments (full red squares) is scattered similar to $\alpha_{\text{HH}}(\text{HCl})$ on
429 crystalline HCl hexahydrate (Iannarelli and Rossi, 2014) up to a factor of 10 for results at the
430 same temperature. We may interpret this result akin to the HCl hexahydrate case where the
431 scatter may be caused by the variability of the surface composition, the morphology or the
432 smoothness of the ice surface (McNeill et al., 2007). Similar results have recently been
433 presented by Moussa et al. (2013) regarding the nitric acid-induced surface disorder on ice. In
434 any case, all results show that $\alpha_{\beta\text{-NAT}}(\text{H}_2\text{O})$ is at least a factor of 10 lower than $\alpha_{\text{ice}}(\text{H}_2\text{O})$ on
435 pure ice in the temperature range 182-200 K.

436 $\alpha_{\beta\text{-NAT}}(\text{H}_2\text{O})$ in TO experiments (empty red squares) on the other hand, increases as a
437 function of temperature in the temperature range 182-198 K varying from 0.013 at 182 K to
438 approximately 0.1 at 198 K, being equal at the highest temperature to $\alpha_{\text{ice}}(\text{H}_2\text{O})$ on pure ice
439 within experimental error. This result is in contrast to Delval and Rossi (2005) who report a
440 negative temperature dependence of $\alpha_{\beta\text{-NAT}}(\text{H}_2\text{O})$ in the temperature range 182-207 K. A
441 possible reason for the different behavior of PV and TO experiments may be intrinsic in the
442 nature of PV experiments: the ice surface is exposed to a series of pulses of H_2O and the free
443 sites may be saturated before the introduction of each consecutive pulse. We suspect this to be
444 the reason for the discrepancy between PV and TO experiments and we will consider the
445 results of TO experiments as the preferred values of this work despite the larger experimental
446 scatter.

447 Like $\alpha_{\beta\text{-NAT}}(\text{H}_2\text{O})$, the values of $\alpha_{\beta\text{-NAT}}(\text{HNO}_3)$ (black empty triangles) increase as a
448 function of temperature in the measured temperature range from a value of approximately
449 0.015 at 182 K to a value of 0.08 at 195.5 K. However, the values have a large estimated
450 uncertainty. These values are lower by a factor of 2 to 10 compared to the preferred values
451 indicated by the IUPAC Subcommittee on Gas Kinetic Data Evaluation (Crowley et al., 2010)
452 in the temperature range 190 to 200 K.

453 Figure 4b shows results for $R_{\text{ev}}(X)$ in $\text{molec s}^{-1} \text{cm}^{-3}$ as a function of temperature. The same
454 symbols as in panel (a) are used. $R_{\text{ev}}(\text{H}_2\text{O})$ on $\beta\text{-NAT}$ in PV experiments is lower by a factor
455 of 50 compared to $R_{\text{ev}}(\text{H}_2\text{O})$ on pure ice in the temperature range 182-200 K. As in the case of

456 α -NAT, this result is very different compared to the case of HCl hydrates studied before using
457 the same apparatus (Iannarelli and Rossi, 2013) where the evaporation of H₂O is not
458 influenced by the presence of adsorbed HCl on the ice and takes place at a rate characteristic
459 of pure ice for all HCl concentrations used.

460 $R_{ev}(H_2O)$ on β -NAT measured using the TO method is close to $R_{ev}(H_2O)$ obtained in PV
461 experiments, the former being approximately a factor of 2 higher. $R_{ev}(HNO_3)$ on β -NAT
462 increases in the temperature range 182-195.5 K with a steeper slope compared to $R_{ev}(H_2O)$,
463 the former being smaller by approximately a factor of 1000 at 182 K and 50 at 196 K
464 compared to $R_{ev}(H_2O)$ of β -NAT. It varies from 2×10^8 at 182 K to 8.5×10^9 molec s⁻¹ cm⁻³ at
465 195.5 K.

466 Figure 4c shows the results for $P_{eq}(X)$ in Torr calculated according to Eq. (9) for both H₂O
467 and HNO₃ as a function of temperature. The same symbols as in panels (a) and (b) are used.
468 $P_{eq}(H_2O)$ of β -NAT calculated from the results of TO experiments is lower by up to a factor
469 of 10 in the middle of the covered T-range compared to $P_{eq}(H_2O)$ of pure ice in the
470 temperature range 182-195.5 K. $P_{eq}(H_2O)$ of β -NAT calculated from the kinetic parameters
471 measured in PV agrees with TO experiments within experimental uncertainty. Saturation
472 effects in PV experiments will affect both the accommodation (α) and evaporation (J_{ev})
473 process to the same extent such that P_{eq} should be invariant to the chosen experimental
474 procedure (PV or TO). However, there is a noticeable scatter in $P_{eq}(H_2O)$ for β -NAT on
475 display in Figure 4c which presumably reflects the range of different compositions of the
476 binary HNO₃/H₂O system. According to Gibb's Phase Rule we have three phases and two
477 components which leads to a single degree of freedom for the system. At constant
478 temperature different HNO₃/H₂O mixing ratios will lead to different values of $P_{eq}(H_2O)$ if we
479 stay on an isotherm. This corresponds to a vertical cut in the binary phase diagram for β -NAT
480 in Figure 5. It shows that we expect $P_{eq}(H_2O)$ values between a factor of ten or so for the
481 experimental points that "fill" the NAT phase diagram more or less homogeneously within
482 the used T range.

483 In addition, Figure 5 shows that the majority of points are in the rectangular shaded area
484 representing polar stratospheric conditions: β -NAT is the stable phase under these conditions
485 and our results agree well with the literature (McElroy et al., 1986; Hamill et al., 1988;
486 Molina, 1994; Koehler et al., 1992). A more complete manner to display the binary phase
487 diagram is presented in Figure S5 (Supplementary Information). It shows both the HNO₃ and

488 H₂O partial pressures in one single plot close to selected isotherms marked by straight
489 intersecting dashed lines. It is immediately apparent that both HNO₃ and H₂O partial
490 pressures are comparable to upper tropospheric/lower stratospheric values.

491 **3.3 HCl kinetics on α -NAT and β -NAT Thin Films**

492 As already mentioned, we used a combination of real-time PV and steady state experiments
493 using HCl as probing gas in order to measure the kinetics of HCl interacting with α -NAT and
494 β -NAT ice films. Figure 6 displays raw data from repetitive pulsed dosing of HCl onto an α -
495 NAT/ice substrate as a function of elapsed time. The lower panel displays the MS signals of
496 HCl (red, m/e 36), H₂O (blue, m/e 18) and HNO₃ (black, m/e 46), respectively, and the
497 individual pulses, of which there were twelve, are identifiable by sharp peaks on top of the red
498 columns. Each pulse corresponds to $(4-5)\times 10^{16}$ molecule resulting in a total HCl dose of
499 approximately 3×10^{17} molecules. This is the dose effectively administered to the α -NAT
500 when the fraction of HCl going to the vessel walls and escaping the SFR has been subtracted.
501 This dose approximately corresponds to 1000 molecular monolayers of HCl adsorbed onto the
502 substrate.

503 The temperature of the cryostat is displayed as the green trace in the lower panel, and with
504 every T-increase the MS steady-state levels of HCl, H₂O and HNO₃ increase concomitantly.
505 (During the pulsed admission of HCl the MS levels of HNO₃ and H₂O are subject to artifacts
506 owing to rapid switching).

507 Turning to the upper panel of Figure 6 we display a series of FTIR transmission spectra from
508 700 to 4000 cm⁻¹ at specific times during the repetitive pulsing experiment which are
509 indicated in the lower panel by a series of color-coded “sp1” and continuing going from red to
510 purple. The principal peak positions have been collected in Table 3 and will be discussed
511 below in terms of changes in the “pure” α -NAT/ice absorption spectra owing to the presence
512 of increasing adsorbed HCl. The enlarged IR-spectral range in the upper panel of Figure 6
513 displays the effect of the HCl adsorption particularly well by showing a non-monotonic
514 sequence of IR absorption peaks not present in the “pure” reference spectra from Iannarelli
515 and Rossi (2015). The raw MS data from the lower panel of Figure 6 have been used to
516 calculate the kinetic and thermodynamic data displayed in Figure 8.

517 Figure 7 displays raw data from repetitive pulsed dosing of HCl onto a β -NAT/ice substrate in
518 analogy to Figure 6. The eleven individual pulses corresponded to $(6-7)\times 10^{16}$ molecule per

519 pulse resulting in a total HCl dose of approximately 4×10^{17} molecules which amounts to
520 1300 molecular monolayers or so. Like in Figure 6 the upper panel displays a series of color-
521 coded FTIR absorption spectra in transmission with the principal peak positions collected in
522 Table 3. As for Figure 6 the MS steady-state levels at the different temperatures will be used
523 to derive the kinetic and thermodynamic data of Figure 9 as a function of temperature.

524 In addition, Figure S6 presents an enlarged graph for the non-exponential decay of a HCl
525 pulse interacting with both α - and β -NAT on a 30 s time scale consisting of a fast and a
526 slowly-decaying portion. The evaluation of such pulsed admission MS signals has been
527 presented in the past (Iannarelli and Rossi, 2014, Supplemental Information (SI)) and the
528 present analysis and fitting of the HCl MS signals follows the same scheme.

529 A look at Table 3 should provide an answer as to whether or not there is an identifiable
530 spectral fingerprint of HCl adsorbed on α - or β -NAT in the FTIR absorption spectrum of the
531 combined α - or β -NAT/HCl system displayed in Figure 6 and Figure 7.

532 The first column of Table 3 reveals the spectral fingerprint of HCl for α -NAT/HCl in terms of
533 additional peaks (*in italics*) that are not present in the reference spectrum (pure α -NAT)
534 recorded using the identical instrument and presented in the third column. There seem to be
535 two spectral regions where the presence of HCl may be apparent, namely in the 1618-1644
536 cm^{-1} region corresponding to the broad bending vibration of the proton-ordered waters of
537 hydration (Ritzhaupt and Devlin, 1991; Martin-Llorente et al., 2006), and more importantly,
538 the band at 1328 cm^{-1} that overlaps with the 1339 cm^{-1} vibration, the latter of which is not
539 changing with increasing HCl dose.

540 The series of FTIR absorption spectra displayed in Figure 6 shows the non-monotonous
541 change of intensity at this transition (1328 cm^{-1}): sp1 (red), sp2 (yellow) and sp3 (green)
542 display the growth of a shoulder to the red of the 1375 cm^{-1} peak, sp4 (turquoise), sp5 (blue)
543 and sp6 (purple) show the separate peak in its decline (1328 cm^{-1}) owing to evaporation of
544 HCl together with NAT.

545 For β -NAT the analogous situation is displayed in the second and fourth column of Table 3
546 and Figure 7. Here the presence of HCl is more discrete within the FTIR absorption spectrum
547 of β -NAT as Table 3 suggests the well-separated peak to the blue of the 3227 cm^{-1} ice peak at
548 3360 cm^{-1} to be a HCl tracer as it looks very similar to the HCl/H₂O system (Iannarelli and
549 Rossi, 2014; Chiesa and Rossi, 2013). The peaks identified to appear in the FTIR spectrum

550 upon HCl adsorption may be found in the fifth column of Table 3 which displays the principal
551 IR peaks in the reference HCl/H₂O system, except the 1200 cm⁻¹ vibration found in column 1
552 and 2 whose origin remains unclear.

553 In order to restrain the number of independent measurements on this ternary system to a
554 practical level we had to make some assumptions and/or simplifications in order to measure
555 the unknown parameters of Eq. (2) for each gas used. Specifically, we made the following
556 reasonable assumptions, both for α -NAT and β -NAT substrates which have been
557 experimentally verified in laboratory experiments:

- 558 • $R_{ev}(H_2O)$ on NAT remains unchanged in the presence of HCl
- 559 • $\alpha_{NAT}(H_2O)$ remains unchanged in the presence of HCl
- 560 • $\alpha_{NAT}(HNO_3)$ remains unchanged in the presence of HCl

561 Under these assumptions, no additional measurements of the heterogeneous kinetics of H₂O
562 in the presence of HCl have been performed. We have measured the steady-state flow
563 $F_{SS}(HNO_3)$ before each HCl pulse series and used previously measured $\alpha_{\alpha-NAT}(HNO_3)$ and
564 $\alpha_{\beta-NAT}(HNO_3)$ from TO experiments on α -NAT and β -NAT phases in order to calculate
565 $R_{ev}(HNO_3)$ and $P_{eq}(HNO_3)$ according to Eqs. (8) and (9) in HCl-PV experiments as well. As a
566 net result we measure or calculate the following kinetic parameters for α -NAT and β -NAT
567 substrates: $R_{ev}(HCl)$, $\alpha_{NAT}(HCl)$ and $R_{ev}(HNO_3)$ in the presence of HCl.

568 Figure 8 displays the results of HCl-PV experiments on α -NAT substrates. Full red diamonds
569 represent the results for HCl whereas full black circles represent HNO₃ results using
570 $\alpha_{\alpha-NAT}(HNO_3)$ from TO experiments and $F_{SS}(HNO_3)$ from HCl-PV experiments. Empty
571 black triangles represent results for HNO₃ in TO experiments reported from Figure 2 for
572 comparison.

573 Figure 8a displays the measured $\alpha_{\alpha-NAT}(X)$ as a function of temperature. $\alpha_{\alpha-NAT}(HCl)$ (full
574 red diamonds) slightly decreases as a function of temperature in the range 177.5-199.5 K,
575 being equal to $\alpha_{ice}(H_2O)$ on pure ice at low temperatures and lower by a factor of 4 at T =
576 199.5 K. The decrease seems to be significant. Values of $\alpha_{\alpha-NAT}(HNO_3)$ measured in TO
577 experiments in the absence of HCl are reported as empty black triangles in agreement with the
578 third above-listed assumptions. We used these values in order to calculate $R_{ev}(HNO_3)$ and
579 $P_{eq}(HNO_3)$ in the presence of HCl.

580 Figure 8b shows results for $R_{ev}(X)$ in $\text{molec s}^{-1} \text{cm}^{-3}$ as a function of temperature. The same
581 symbols as in panel (a) are used. $R_{ev}(\text{HCl})$ on α -NAT slightly increases as a function of
582 temperature, but is lower by a factor of 1000 in the measured temperature range 177.5-199.5
583 K compared to $R_{ev}(\text{H}_2\text{O})$ on pure ice. $R_{ev}(\text{HNO}_3)$ increases as a function of temperature,
584 varying from 1×10^8 at 181 K to 9×10^9 $\text{molec s}^{-1} \text{cm}^{-3}$ at 189 K. The presence of HCl does not
585 have any effect on the rate of evaporation of HNO_3 from α -NAT films: we observe no
586 increase of $F_{ss}(\text{HNO}_3)$ following HCl pulses and $R_{ev}(\text{HNO}_3)$ in the presence of adsorbed HCl
587 molecules (full black circles) is identical within experimental error to $R_{ev}(\text{HNO}_3)$ of α -NAT
588 films free of adsorbed HCl (empty black triangles). However, this result is contingent upon
589 the assumptions listed before, namely $\alpha_{\alpha\text{-NAT}}(\text{HNO}_3)$ being independent of the presence or
590 absence of HCl.

591 Figure 8c shows the results for $P_{eq}(X)$ in Torr calculated according to Eq. (9) for both HCl and
592 HNO_3 as a function of temperature. The same symbols as in panel (a) and (b) are used.
593 $P_{eq}(\text{HCl})$ for HCl-doped α -NAT is lower by a factor of approximately 100 compared to
594 $P_{eq}(\text{H}_2\text{O})$ on pure ice in the measured temperature range. A comparison with the results of
595 $P_{eq}(\text{HCl})$ of crystalline HCl hexahydrate and amorphous HCl/ H_2O mixtures calculated using
596 the same experimental methodology (Iannarelli and Rossi, 2014) shows that $P_{eq}(\text{HCl})$ of HCl-
597 doped α -NAT is lower by a factor of approximately 10 compared to $P_{eq}(\text{HCl})$ of crystalline
598 hexahydrate in the overlapping temperature range (177.5-193.5 K).

599 $P_{eq}(\text{HCl})$ of amorphous HCl/ H_2O mixtures is higher by a factor of 20 compared to $P_{eq}(\text{HCl})$ of
600 HCl-doped α -NAT at low temperatures (177.5 K) with the difference being constant or
601 slightly decreasing at high temperatures (199.5 K) where $P_{eq}(\text{HCl})$ of the amorphous mixture
602 is only a factor of 4 higher than $P_{eq}(\text{HCl})$ of α -NAT.

603 $P_{eq}(\text{HNO}_3)$ on HCl-doped α -NAT films is equal within experimental error to $P_{eq}(\text{HNO}_3)$ of α -
604 NAT films free of adsorbed HCl. It is lower by a factor of 1000 compared to $P_{eq}(\text{H}_2\text{O})$ on
605 pure ice in the measured temperature range 177.5-199.5 K.

606 Figure 9a (symbols have the same meaning as in Figure 8) shows the measured values of
607 $\alpha_{\beta\text{-NAT}}(X)$ as a function of temperature. $\alpha_{\beta\text{-NAT}}(\text{HCl})$ slightly decreases as a function of
608 temperature in the range 177-201 K, varying from 0.025 at 177 K to 0.016 at 201 K which
609 may or may not be significant. As for the case of α -NAT, we assume that $\alpha_{\beta\text{-NAT}}(\text{HNO}_3)$

610 (empty black triangles) equals the measured values of $\alpha_{\beta\text{-NAT}}(\text{HNO}_3)$ on HCl-free β -NAT in
611 two-orifice experiments whose results are displayed in Figure 4a.

612 Figure 9b shows results for the $R_{\text{ev}}(\text{X})$ in $\text{molec s}^{-1} \text{cm}^{-3}$ as a function of temperature. The
613 same symbols as in Panel (a) are used. $R_{\text{ev}}(\text{HCl})$ on β -NAT is equal at higher temperature
614 within experimental uncertainty to $R_{\text{ev}}(\text{HCl})$ on α -NAT and is lower by a factor of 1000 in the
615 temperature range 177- 201 K compared to $R_{\text{ev}}(\text{H}_2\text{O})$ on pure ice. $R_{\text{ev}}(\text{HNO}_3)$ on HCl-doped
616 β -NAT films, being equal within experimental error to $R_{\text{ev}}(\text{HNO}_3)$ of undoped β -NAT films,
617 indicates that adsorbed HCl molecules seem to have no effect on the rate of evaporation of
618 HNO_3 from β -NAT films in the presence of HCl as well, at least in the given T range.

619 Figure 9c shows the results for $P_{\text{eq}}(\text{X})$ in Torr calculated according to Eq. (9) for both HCl and
620 HNO_3 as a function of temperature. The same symbols as in panel (a) and (b) are used.
621 $P_{\text{eq}}(\text{HCl})$ of HCl-doped β -NAT is lower by a factor of approximately 100 compared to
622 $P_{\text{eq}}(\text{H}_2\text{O})$ on pure ice. $P_{\text{eq}}(\text{HCl})$ of HCl-doped β -NAT is identical within experimental
623 uncertainty to $P_{\text{eq}}(\text{HCl})$ of HCl-doped α -NAT in the measured temperature range 177-201 K
624 and the same observations are valid when comparing $P_{\text{eq}}(\text{HCl})$ of crystalline HCl hexahydrate
625 with amorphous HCl/ H_2O mixtures (Iannarelli and Rossi, 2014).

626 **4 Discussion**

627 In this work we have been able to grow HNO_3 hydrates at temperatures relevant to the
628 stratosphere with tight control on the deposition conditions whose details have been published
629 by Iannarelli and Rossi (2015) as far as the mass balance is concerned. Spontaneous
630 crystallization of α -NAT film on pure ice has been observed upon HNO_3 deposition. Under
631 the present conditions β -NAT was never observed to crystallize directly upon HNO_3
632 deposition but was always obtained as the stable form after conversion of α -NAT films.
633 Temperatures higher than 185 K are necessary for the conversion to occur on the time scale of
634 the experiments we have performed.

635 $\alpha_{\alpha\text{-NAT}}(\text{H}_2\text{O})$ shows two distinct temperature dependent regimes. At temperatures lower than
636 180-185 K it decreases as a function of temperature reaching a minimum of approximately
637 0.003 at 185 K as displayed in Figure 2a. For temperatures higher than 185 K, $\alpha_{\alpha\text{-NAT}}(\text{H}_2\text{O})$
638 increases as a function of temperature, being equal to $\alpha_{\text{ice}}(\text{H}_2\text{O})$ on pure ice and $\alpha_{\beta\text{-NAT}}(\text{H}_2\text{O})$
639 at 193.5 K. An Arrhenius representation of the evaporative flux $J_{\text{ev}}(\text{H}_2\text{O})$ (see Table 1) on α -
640 NAT shows two distinct regimes of temperature dependence, as well. Figure 10 reports the

641 results for PV and TO experiments as full and empty red circles, respectively. We keep the
642 two data sets separated for clarity, but the results of PV and TO experiments are
643 indistinguishable within experimental uncertainty in the measured temperature range.

644 Eqs. (11) and (12) present the two-parameter representations of the Arrhenius lines for
645 $J_{\text{ev}}(\text{H}_2\text{O})$ displayed in Figure 10. Equations (11) and (12) represent the solid and dashed red
646 lines, respectively, with $R = 8.314 \text{ J K}^{-1} \text{ mol}^{-1}$ used throughout:

$$647 \quad 181 \text{ K} \leq T \leq 193.5 \text{ K: } \log J_{\text{ev}}(\text{H}_2\text{O})[\text{molec} \cdot \text{cm}^{-2} \cdot \text{s}^{-1}] = (35.9 \pm 2.8) - \frac{(75.3 \pm 9.9) \times 10^3}{2.303 RT} \quad (11)$$

$$649 \quad 167 \text{ K} \leq T \leq 181 \text{ K: } \log J_{\text{ev}}(\text{H}_2\text{O})[\text{molec} \cdot \text{cm}^{-2} \cdot \text{s}^{-1}] = (15.1 \pm 1.2) - \frac{(3.5 \pm 4.2) \times 10^3}{2.303 RT} \quad (12)$$

650 Table 4 reports a synopsis of the kinetic (J_{ev}) as well as the thermodynamic (P_{eq}) parameters
651 calculated for all experiments of the present work.

652 The considerable scatter in the kinetic data, reflected in the significant uncertainties of Eqs.
653 (11) and (12), may be explained by the variability of the surface composition of the film as
654 well as the surface roughness and surface disorder of the ice substrates, in analogy to the HCl
655 case (Iannarelli and Rossi, 2014). For HCl the scatter in the kinetic data was thought to be
656 due to the stochastic nature of crystal growth of hexahydrate films compared to amorphous
657 mixtures of HCl/H₂O of similar composition and does not represent a lack of reproducibility.

658 Moussa et al. (2013) have observed variations of up to a factor of 10 of the HNO₃ vapor
659 pressure of “smooth” ice samples exposed to HNO₃ as a result of induced surface disorder.
660 The exposure of the present samples to repeated high H₂O supersaturation during PV
661 experiments may lead to surface increased disorder due to liquefaction and/or reconstruction.
662 In the high temperature regime we calculate an activation energy for H₂O evaporation
663 $E_{\text{ev}}(\text{H}_2\text{O}) = (75.3 \pm 9.9) \text{ kJ mol}^{-1}$, and in the low temperature regimes almost no temperature
664 dependence is observed with an activation energy for H₂O evaporation of $E_{\text{ev}}(\text{H}_2\text{O}) = (3.5 \pm$
665 $4.2) \text{ kJ mol}^{-1}$.

666 The discontinuity in the Arrhenius representation of kinetic parameters has already been
667 observed in pure ice as reported by Chaix et al. (1998); Delval et al. (2003); Delval and Rossi
668 (2004); Pratte et al. (2006). The temperatures at which the discontinuity occurs are higher in
669 previous work: Delval et al. (2003) reported a discontinuity at approximately 208 K in their
670 work on H₂O evaporation from HCl and HBr doped ice substrates. In a quartz crystal
671 microbalance study of H₂O evaporation from pure ice the change in slope is reported at $193 \pm$

672 2 K (Delval and Rossi, 2004) comparable with the temperature of 188 ± 2 K reported by
673 Pratte et al. (2006) in their work on the kinetics of H₂O evaporation and condensation on
674 different types of ice.

675 No clear explanation for this break has yet been advanced. The discontinuity may be an
676 indication of the formation of a new disordered structure similar to the quasi-liquid layer
677 induced by HCl as proposed by McNeill et al. (2006). The observation of the break in pure ice
678 samples as well, however, strongly suggests that the onset of a quasi-liquid layer may be
679 independent of the presence of HCl and that the history and evolution of the sample play a
680 role in the arrangement of the structure, similarly to the case of the presence of cubic ice at
681 high temperature in common hexagonal ice that finally turned out to be a perturbed hexagonal
682 ice structure (Kuhs et al., 2012).

683 In the case of β -NAT we have good agreement between PV (dotted line) and TO (solid line)
684 experiments of $P_{eq}(H_2O)$ as shown in the van 't Hoff representation displayed in Figure 11.

685 As already mentioned, the ice surface is exposed to a series of pulses of H₂O during PV
686 experiments. The free sites may be saturated before the introduction of each consecutive pulse
687 resulting in the discrepancy between PV and TO experiments. We therefore believe that the
688 results from PV experiments are more precise but less accurate owing to partial surface
689 saturation whereas the TO experiments are less precise but more accurate. We chose the latter
690 as the preferred values of this work despite the larger scatter in the data compared to the PV
691 experiments.

692 Eqs. (13) and (14) reports the best linear fit for TO and PV experiments on β -NAT displayed
693 in Figure 11, respectively:

$$694 \log P_{eq}(H_2O)[Torr] = (16.7 \pm 4.9) - \frac{(76.7 \pm 17.7) \times 10^3}{2.303 RT} \quad \text{TO - Preferred} \quad (13)$$

$$695 \log P_{eq}(H_2O)[Torr] = (16.7 \pm 3.0) - \frac{(75.5 \pm 11.1) \times 10^3}{2.303 RT} \quad \text{PV} \quad (14)$$

696 The enthalpies of evaporation of H₂O on β -NAT films calculated for the two measurement
697 techniques are $\Delta H_{ev,TO}^0(H_2O) = (76.7 \pm 17.7)$ kJ mol⁻¹ for TO and $\Delta H_{ev,PV}^0(H_2O) = (75.5 \pm$
698 $11.1)$ kJ mol⁻¹ for PV experiments, respectively. The results show good agreement between
699 the two experimental techniques despite the experimental scatter. The average value of
700 $\Delta H_{ev}^0(H_2O) = (76.1 \pm 14.4)$ kJ mol⁻¹ is slightly higher, as expected, but not significantly
701 different compared to α -NAT films. Figure S2 of Supplement C displays a van't Hoff plot for

702 α -NAT with $\Delta H_{\text{ev}}^0(\text{H}_2\text{O}) = (70.3 \pm 14.1)$ and (56.5 ± 5.1) kJ mol⁻¹ for TO and PV
 703 experiments, respectively. Both values are identical within experimental uncertainty whose
 704 average yields $\Delta H_{\text{ev}}^0(\text{H}_2\text{O}) = (63.4 \pm 9.6)$ kJ mol⁻¹ and which leads to a standard enthalpy of
 705 formation slightly larger than that for β -NAT, as expected.

706 However, we do not have good agreement between TO and PV experiments for the kinetic
 707 parameters of β -NAT: a discrepancy is observed in the results of the two measurement
 708 techniques regarding $R_{\text{ev}}(\text{H}_2\text{O})$ and $\alpha(\text{H}_2\text{O})$ for β -NAT. Figure 4 already shows a discrepancy
 709 in $\alpha(\text{H}_2\text{O})$ (full and empty red squares in panel a) with the results of TO experiments being
 710 larger by a factor of approximately 5 at 185 K increasing to a factor of 100 at 200 K compared
 711 to PV experimental results across the whole temperature range. The same qualitative trend,
 712 albeit to a smaller extent, is observed for $R_{\text{ev}}(\text{H}_2\text{O})$ (Figure 4b) and the Arrhenius
 713 representation of $J_{\text{ev}}(\text{H}_2\text{O})$ on β -NAT clearly shows the discrepancy between the different
 714 measurement techniques.

715 The two-parameter representations of the Arrhenius lines displayed in Figure 12 for β -NAT
 716 are reported in Eqs. (15) and (16) for TO (solid line) and PV (dotted line) experiments,
 717 respectively:

$$718 \log J_{\text{ev}}(\text{H}_2\text{O})[\text{molec} \cdot \text{cm}^{-2} \cdot \text{s}^{-1}] = (36.0 \pm 1.3) - \frac{(77.0 \pm 4.9) \times 10^3}{2.303 RT} \text{ TO - Preferred} \quad (15)$$

$$719 \log J_{\text{ev}}(\text{H}_2\text{O})[\text{molec} \cdot \text{cm}^{-2} \cdot \text{s}^{-1}] = (28.7 \pm 0.7) - \frac{(52.1 \pm 2.4) \times 10^3}{2.303 RT} \text{ PV} \quad (16)$$

720 Contrary to the case of α -NAT, no discontinuity in $J_{\text{ev}}(\text{H}_2\text{O})$ has been observed in the
 721 Arrhenius plot of β -NAT displayed in Figure 12. We attribute the discrepancy between PV
 722 and TO experiments to the fact that the former may be subject to partial saturation of uptake
 723 and evaporation in the aftermath of transient supersaturation (PV). A look at the results of
 724 $\alpha_{\alpha\text{-NAT}}(\text{H}_2\text{O})$ in Figure 2a reveals that the results of the TO measurement technique agrees
 725 well with the PV technique in the overlapping temperature range. However, this plot displays
 726 a “hole” of a factor of 20 centered in the neighborhood of $T = 180 \pm 3$ K with respect to the
 727 values at the fringes of the temperature interval. There are indications that PV experiments on
 728 α -NAT substrates may yield lower values of $\alpha_{\alpha\text{-NAT}}(\text{H}_2\text{O})$ at high temperatures in excess of
 729 approximately 182 K (Figure 2a), similarly to the results for $\alpha_{\beta\text{-NAT}}(\text{H}_2\text{O})$ for a β -NAT film
 730 (Figure 4a). This might be an indication that PV experiments are very sensitive to the
 731 interfacial nature of the sample. In other words, transient supersaturation (PV) and “passive”

732 steady-state (TO) experiments may address different properties of the gas-condensed surface
733 interface. This is the first time such a large discrepancy between two kinetic measurements
734 techniques has been observed. As expected, thermodynamic results are not affected for
735 reasons of microscopic reversibility because both forward ($\alpha(\text{H}_2\text{O})$) and reverse reactions
736 ($J_{\text{ev}}(\text{H}_2\text{O})$) are affected to the same extent which cancels out for the calculation of the values
737 of thermodynamic parameters.

738 Figure S3 of Supplement C shows the results of PV experiments using H_2O as a probe gas on
739 α -NAT and β -NAT substrates. Red and black circles represent the decay of series of two
740 pulses on α - and β -NAT, respectively, with the first and second pulse labeled accordingly. In
741 the case of α -NAT films (red circles), the decay of the second pulses is equal to within 20-
742 30% of the decay of the initial pulses, and only in a few cases at temperatures higher than 180
743 K is the decay of the second pulse significantly slower than the initial pulse. In the case of β -
744 NAT films, the decay of second pulses is consistently slower than the decay of first pulses in
745 most cases. This indicates that the surface of β -NAT films exposed to a transient
746 supersaturation of H_2O vapor is more prone to saturation compared to α -NAT.

747 As mentioned before, we consider the results of TO experiments preferred for β -NAT this
748 work despite its larger uncertainty. The enthalpies of evaporation $\Delta H_{\text{ev,TO}}^0(\text{H}_2\text{O}) = (76.7 \pm$
749 $17.7) \text{ kJ mol}^{-1}$ and the activation energy for evaporation $E_{\text{ev}}(\text{H}_2\text{O}) = (77.0 \pm 4.9) \text{ kJ mol}^{-1}$ are
750 equal to within experimental uncertainties. We calculate an activation energy of
751 accommodation for H_2O on β -NAT of $E_{\text{acc}}(\text{H}_2\text{O}) = E_{\text{ev}}(\text{H}_2\text{O}) - \Delta H_{\text{ev,TO}}^0(\text{H}_2\text{O}) = 0$. Therefore,
752 no activation energy is required for the accommodation process of H_2O on β -NAT which is an
753 expected experimental outcome. In contrast, the activation energy for H_2O accommodation on
754 α -NAT is computed as $E_{\text{acc}}(\text{H}_2\text{O}) = E_{\text{ev}}(\text{H}_2\text{O}) - \Delta H_{\text{ev,average}}^0(\text{H}_2\text{O}) = 75.3 - 63.4 = 11.9$
755 kJ/mol when using a value averaged over the PV and TO experiment of 63.4 kJ/mol for
756 $\Delta H_{\text{ev,average}}^0(\text{H}_2\text{O})$. This small, but possibly significant positive activation energy is
757 consistent with the positive temperature dependence of $\alpha_{\alpha\text{-NAT}}(\text{H}_2\text{O})$ displayed in Figure 2a
758 for the TO experiment at $T > 182 \text{ K}$, that is in the high T-range.

759 $R_{\text{ev}}(\text{H}_2\text{O})$ on both α -NAT and β -NAT is smaller compared to $R_{\text{ev}}(\text{H}_2\text{O})$ on pure ice. This is in
760 agreement with the results of Tolbert and Middlebrook (1990), Middlebrook et al. (1996),
761 Warshawsky et al. (1999) and Delval and Rossi (2005) who showed that ice coated with a
762 number of molecular layers of NAT evaporates H_2O at a slower rate than pure ice. On the

763 other hand, our results are in contrast with the findings of Biermann et al. (1998) who report
764 that no significant decrease of the H₂O evaporation rate was observed in HNO₃-doped ice
765 films. The discrepancy may possibly be caused by the high total pressure of 0.85 mbar in their
766 reactor compared to all other competitive studies cited above that use high-vacuum chambers
767 with total pressures lower by typically a factor of 500 or more.

768 It is very likely that the experiments performed by Biermann et al. (1998) were not sensitive
769 to changes in evaporation rates despite the fact that both the HNO₃ and H₂O concentrations
770 used as well as the thickness of the accumulated NAT layers in their no. 5 experiment were of
771 the same magnitude as in the competing studies. A hint to that effect is the unexpected time
772 dependence of the ice evaporation rate in Biermann et al. (1998) that shows an induction time
773 of 30 minutes as opposed to the expected linear decrease from the beginning of evaporation
774 (see below). We are unable to attribute the source of the measured H₂O vapor in the presence
775 of two H₂O-containing solid phases in our chemical system, namely pure H₂O ice and NAT.
776 We restate that the partial pressures at constant temperature are controlled by the (relative)
777 composition of the system in agreement with the single degree of freedom resulting from
778 Gibb's Phase Rule and the data displayed in the binary HNO₃/H₂O phase diagrams displayed
779 in Figure 3, Figure 5 and Figure S5.

780 Delval and Rossi (2005) report that the initial evaporation of H₂O in their experiments was
781 always that of pure ice and that R_{ev}(H₂O) gradually decreases with the evaporation of excess
782 H₂O and the increase in the average HNO₃ mole fraction. They refer to this difference as
783 "high and low evaporation rate" regime of H₂O. Our observation is somewhat different
784 compared to Delval and Rossi (2005): R_{ev}(H₂O) on α-NAT and β-NAT is smaller compared
785 to R_{ev}(H₂O) on pure ice over the whole temperature range and for all samples. The reason lies
786 in the fact that the average mole fraction of HNO₃ of the present samples is higher by at least
787 a factor of 10 compared to the one used by Delval and Rossi (2005). Therefore all our
788 samples are in the "low evaporation rate" regime of H₂O and our results compare well with
789 the results of Delval and Rossi (2005) once they evaporate excess H₂O and reach the "low
790 evaporation rate" regime.

791 Figure 13 displays both the Arrhenius plots of J_{ev}(HNO₃) (A) and the van 't Hoff plots of
792 P_{eq}(HNO₃) (B) for the interaction of HNO₃ with α- and β-NAT films. We would like to
793 briefly remind the reader that only TO experiments were possible for HNO₃ experiments
794 because no sharp pulses could be generated with pure HNO₃, presumably owing to the

795 tendency of nitric acid to stick to the inner surfaces, mainly on stainless (austenitic) steel. This
 796 has been verified by measuring the Langmuir adsorption on that same surface (Figure S1,
 797 Table 2). The following equations define the corresponding straight lines based on the present
 798 measurements. For α -NAT (Eqs. (17) and (18)) and β -NAT (Eqs. (19) and (20)) films we find
 799 the following results:

$$800 \quad \alpha\text{-NAT:} \quad \log J_{\text{ev}}(\text{HNO}_3)[\text{molec} \cdot \text{cm}^{-2} \cdot \text{s}^{-1}] = (62.3 \pm 7.8) - \frac{(178.0 \pm 27.4) \times 10^3}{2.303 RT} \quad (17)$$

$$801 \quad \log P_{\text{eq}}(\text{HNO}_3)[\text{Torr}] = (29.3 \pm 12.0) - \frac{(128.6 \pm 42.4) \times 10^3}{2.303 RT} \quad (18)$$

$$802 \quad \beta\text{-NAT:} \quad \log J_{\text{ev}}(\text{HNO}_3)[\text{molec} \cdot \text{cm}^{-2} \cdot \text{s}^{-1}] = (40.6 \pm 2.4) - \frac{(102.0 \pm 8.6) \times 10^3}{2.303 RT} \quad (19)$$

$$803 \quad \log P_{\text{eq}}(\text{HNO}_3)[\text{Torr}] = (19.8 \pm 3.3) - \frac{(96.5 \pm 12.0) \times 10^3}{2.303 RT} \quad (20)$$

804 We calculate an activation energy for HNO_3 evaporation on α -NAT and β -NAT of
 805 $E_{\text{ev}}(\text{HNO}_3) = (178.0 \pm 27.4) \text{ kJ mol}^{-1}$ and $E_{\text{ev}}(\text{HNO}_3) = (102.0 \pm 8.6) \text{ kJ mol}^{-1}$, respectively.
 806 These values are higher compared to $E_{\text{ev}}(\text{HCl}) = (87.0 \pm 17) \text{ kJ mol}^{-1}$, the activation energy
 807 for HCl evaporation on hexahydrate. This result is within expectation given the higher
 808 hydrogen bond energy of HNO_3 compared to HCl with H_2O .

809 Similar to the case of H_2O , no activation energy for accommodation of HNO_3 on β -NAT is
 810 required since the evaporation activation energy $E_{\text{ev}}(\text{HNO}_3) = (102.0 \pm 8.6) \text{ kJ mol}^{-1}$ and the
 811 enthalpy of evaporation $\Delta H_{\text{ev}}^0(\text{HNO}_3) = (96.5 \pm 12.0) \text{ kJ mol}^{-1}$ are equal within experimental
 812 uncertainty. In contrast, a substantial activation energy of HNO_3 mass accommodation of 49.4
 813 kJ/mol is calculated from $E_{\text{acc}}(\text{HNO}_3) = E_{\text{ev}}(\text{HNO}_3) - \Delta H_{\text{ev}, \text{TO}}^0(\text{HNO}_3) = 178.0 - 128.6 = 49.9$
 814 kJ/mol which may have to do with the fact that α -NAT is metastable owing to its unstable
 815 H_2O crystal structure (Weiss et al., 2016).

816 The thermodynamic parameters obtained above, namely $\Delta H_{\text{ev}}^0(\text{H}_2\text{O})$ and $\Delta H_{\text{ev}}^0(\text{HNO}_3)$ for
 817 both α - and β -NAT may now be used to estimate the relative stability of α - vs. β -NAT as
 818 follows. The evaporation/condensation equilibrium for both forms of NAT may be
 819 represented in equation (21) where $\Sigma \Delta H_{\text{ev}}^0 = 3 \Delta H_{\text{ev}}^0(\text{H}_2\text{O}) + \Delta H_{\text{ev}}^0(\text{HNO}_3)$ in agreement with
 820 the relevant stoichiometry:



822 For α - and β -NAT we obtain $\Sigma\Delta H_{\text{ev}}^{0,\alpha}$ and $\Sigma\Delta H_{\text{ev}}^{0,\beta}$ equal to 318.8 and 324.8 kJ/mol,
823 respectively, when we use the average of the TO and PV experiment for H_2O and the TO
824 value listed above for HNO_3 evaporation. Specifically, we have used (63.4 ± 9.6) and $(128.6$
825 $\pm 42.2)$ for H_2O - and (76.1 ± 14.4) and (96.5 ± 12.0) for HNO_3 -evaporation for α - and β -
826 NAT, respectively, as displayed above. Finally, we arrive at the difference $\Sigma\Delta H_{\text{ev}}^{0,\alpha} -$
827 $\Sigma\Delta H_{\text{ev}}^{0,\beta} = -6.0 \pm 20.0$ kJ/mol which shows that β -NAT is marginally more stable than α -
828 NAT. This is true despite the fact that the standard heat of evaporation for HNO_3 in α -NAT
829 ($\Delta H_{\text{ev}}^0(\text{HNO}_3)$) is significantly larger than for β -NAT by 32.1 kJ/mol which may be expressed
830 by the fact that the calculated “affinity” of HNO_3 towards ice in the α -NAT is larger than for
831 β -NAT as claimed by Weiss et al. (2016). However, this fact only addresses the behavior of
832 HNO_3 without taking into consideration the partial stability of the H_2O network in the total
833 crystal structure. In view of the large uncertainty, mainly brought about by the TO
834 experiment, we regard this result as an estimate to the true standard enthalpy difference
835 between α - and β -NAT.

836 The results of HCl kinetic measurements displayed in Figure 8 and Figure 9 show that
837 $R_{\text{ev}}(\text{HCl})$ is always higher than $R_{\text{ev}}(\text{HNO}_3)$, with the latter being equal regardless of the
838 presence of absorbed HCl molecules in the condensed phase. Hynes et al. (2002) observed
839 that HCl uptake on HNO_3 dosed ice was always nearly reversible in their experiments, in
840 contrast to HCl uptake on clean ice. Although the same HNO_3 dosed ice surface has been
841 dosed repeatedly at different HCl concentrations by Hynes et al. (2002), the degree of
842 reversibility was found to be unaffected by previous experiments. In contrast, we never
843 observed such reversibility. In our experiments, HCl always remained on the surface,
844 evaporating at a rate only slightly faster than HNO_3 both for α -NAT and β -NAT and similarly
845 to $R_{\text{ev}}(\text{HCl})$ of crystalline hexahydrate (Iannarelli and Rossi, 2014). However, a possible
846 influence of the temperature cannot be excluded at this time, as the experiments performed by
847 Hynes et al. (2002) have been performed at distinctly higher temperatures, namely in the
848 range 210-235 K, compared to the experiments discussed here.

849 Similar behavior has been observed by Kuhs et al. (2012) with respect to the presence of
850 cubic ice or “ice I_c ” in common hexagonal ice I_h . I_h is expected to be the prevalent ice phase at
851 temperatures relevant to atmospheric processing on thermodynamic grounds. Apparent
852 formation of I_c has been observed over a wide temperature range and evidence pointed
853 towards the fact that the resulting phase is not pure cubic ice but instead composed of

854 disordered cubic and hexagonal stacking sequences. Kuhs et al. (2012) studied the extent and
855 relevance of the stacking disorder using both neutron as well as X-ray diffraction as indicators
856 of the “cubicity” of vapor deposited ice at temperatures from 175 to 240 K and could simply
857 not find proof for the formation of cubic ice I_c under atmospheric conditions.

858 Kuhs et al. (2012) discovered that even at temperatures as high as 210 K, the fraction of cubic
859 sequences in vapor deposited ice is still approximately 40%. The rate of decrease in cubicity
860 depends on the temperature, being very slow at temperatures lower than 180 K and
861 increasingly rapid at temperatures higher than 185 K. Furthermore, even at high temperatures
862 the complete transformation into pure ice I_h was never observed, with a few percent of cubic
863 stacking sequences still remaining in the ice, even after several hours at 210 K and
864 disappeared only upon heating to 240 K. In addition, the combination of neutron and X-ray
865 diffraction experiments of Kuhs et al. (2012) cannot distinguish the difference between the
866 bulk and the interface whereas our measurement techniques, in particular PV experiments, are
867 very sensitive to the nature and properties of the sample interface.

868 In light of these results we speculate that the presence of two hydrates of HNO_3 , namely α -
869 NAT and β -NAT, may depend on the cubicity or stack-disorder of the ice upon which the
870 NAT grows. HNO_3 adsorbed on cubic ice I_c tends to form α -NAT crystalline structures which
871 upon heating converts to β -NAT while the ice loses part of its cubicity. The temperature at
872 which the conversion from α -NAT to β -NAT is accelerated, $T = 185$ K, is the same
873 temperature Kuhs et al. (2012) report as the temperature at which the rate of decrease in
874 cubicity increases. Our hypothesis is that the formation of α -NAT or β -NAT may highly
875 depend on the environment in which the NAT phase grows and on the presence of high or low
876 fractions of “ I_c ”.

877 Figure 14 displays both the Arrhenius plots of $J_{ev}(HCl)$ (A) and the van ‘t Hoff plots of
878 $P_{eq}(HCl)$ (B) for the interaction of HCl with α -NAT and β -NAT films. As for the case of
879 HNO_3 , only TO experiments were performed with HCl as a probe gas. Full red circles and
880 black triangles represent the interaction of HCl with α - and β -NAT films, respectively.

881 The following equations define the corresponding straight lines resulting from the present
882 measurements. For α -NAT (Eqs. (22) and (23)) and β -NAT films (Eqs. (24) and (25)) we find
883 the following results:

884 α -NAT:
$$\log J_{ev}(HCl)[\text{molec} \cdot \text{cm}^{-2} \cdot \text{s}^{-1}] = (34.8 \pm 5.3) - \frac{(78.3 \pm 19.2) \times 10^3}{2.303 RT} \quad (22)$$

$$885 \quad \log P_{\text{eq}}(\text{HCl})[\text{Torr}] = (15.7 \pm 3.2) - \frac{(78.4 \pm 11.4) \times 10^3}{2.303 RT} \quad (23)$$

$$886 \quad \beta\text{-NAT:} \quad \log J_{\text{ev}}(\text{HCl})[\text{molec} \cdot \text{cm}^{-2} \cdot \text{s}^{-1}] = (28.6 \pm 1.3) - \frac{(56.7 \pm 4.6) \times 10^3}{2.303 RT} \quad (24)$$

$$887 \quad \log P_{\text{eq}}(\text{HCl})[\text{Torr}] = (13.3 \pm 1.6) - \frac{(69.6 \pm 5.8) \times 10^3}{2.303 RT} \quad (25)$$

888 Despite the considerable scatter of the data displayed in Figure 14 it may be pointed out that
 889 the enthalpy of HCl evaporation is identical for α - and β -NAT within the stated experimental
 890 uncertainty: We compare $\Delta H_{\text{ev}}^0(\text{HCl})$ of 78.4 ± 11.4 and 69.6 ± 5.8 kJ/mol for α - and β -NAT
 891 (equations (23) and (25)). On the other hand, we have equality, perhaps fortuitously, between
 892 $E_{\text{ev}}(\text{HCl})$ and $\Delta H_{\text{ev}}^0(\text{HCl})$ for α -NAT following equations (22) and (23) which leads to the
 893 conclusion that HCl accommodation on α -NAT is not an activated process with essentially
 894 zero activation energy similar to the situation for HNO_3 interacting with β -NAT. On the other
 895 hand, this type of argument would lead to a negative activation energy for HCl
 896 accommodation on β -NAT because the enthalpy of evaporation of HCl from β -NAT is
 897 smaller than $E_{\text{ev}}(\text{HCl})$ from β -NAT.

898 However, the kinetic data of $J_{\text{ev}}(\text{HCl})$ for β -NAT may be affected by saturation of HCl uptake
 899 because experiments have been performed using the PV admission. This situation may be
 900 similar to the kinetic results of $J_{\text{ev}}(\text{H}_2\text{O})$ for β -NAT displayed in Figure 12 that shows a
 901 significantly smaller value for $E_{\text{ev}}(\text{H}_2\text{O})$ in PV vs. TO experiments (52.1 vs. 75.5 kJ/mol, see
 902 also Table 4) whereas the saturation effect seems not to affect the kinetic data for α -NAT.
 903 The anomalously large experimental uncertainty for HNO_3 TO experiments on α -NAT
 904 displayed in Table 4 certainly has to do with the restricted temperature interval over which we
 905 were able to monitor α -NAT before it converted to β -NAT. This may be seen in the synoptic
 906 overview of the van't Hoff plots for HNO_3 interacting with NAT displayed in Figure S4 of
 907 Supplement D. This restricted T range is also visible in Figure 13A for $J_{\text{ev}}(\text{HNO}_3)$ from α -
 908 NAT..

909 **5 Atmospheric implications and conclusion**

910 In this study we have confirmed that exposure of ice films to HNO_3 vapor pressures at
 911 temperatures found in the stratosphere leads to formation of NAT hydrates.

912 Of the two known forms of NAT, namely α -NAT and β -NAT, the latter is the
913 thermodynamically stable one whereas metastable α -NAT is likely to be of lesser importance
914 in the heterogeneous processes at UT/LS atmospherically relevant conditions.

915 $R_{\text{ev}}(\text{H}_2\text{O})$ on α -NAT and β -NAT films are very different compared to the case of HCl/ice
916 where the evaporation of H_2O is not influenced by the presence of adsorbed HCl on the ice
917 and takes place at a rate characteristic of pure ice. This has important implications on the
918 lifetime of atmospheric ice particles. Ice particles with adsorbed HNO_3 forming NAT have
919 longer lifetimes compared to ice particles with adsorbed HCl, being amorphous or crystalline
920 $\text{HCl}\cdot 6\text{H}_2\text{O}$. In light of our results we raise the question if HCl-containing ice particles are of
921 significant atmospheric relevance as substrates for heterogeneous reactions due to their
922 reduced lifetimes and concurrent reduced opportunities to enable heterogeneous atmospheric
923 reactions such as Reaction (1).

924 $J_{\text{ev}}(\text{H}_2\text{O})$ on α -NAT presents a discontinuity at 185 K akin to that observed in pure ice by
925 Delval and Rossi (2004); Pratte et al. (2006). The resulting Arrhenius representation at high
926 temperatures larger than 181 ± 2 K is:

$$927 \log J_{\text{ev}}(\text{H}_2\text{O})[\text{molec} \cdot \text{cm}^{-2} \cdot \text{s}^{-1}] = (35.9 \pm 2.8) - \frac{(75.3 \pm 9.9) \times 10^3}{2.303 RT} \quad (11)$$

928 $J_{\text{ev}}(\text{H}_2\text{O})$ on β -NAT shows two values depending on the measurement techniques as a result of
929 the propensity of the PV experiment to saturate the gas-condensate interface. TO experiments
930 are less precise but more accurate owing to the fact that they are less prone to saturation
931 compared to PV experiments. Therefore, we report results of TO experiments as preferred
932 values, whereas we rule out kinetic PV results owing to possible saturation problems and note
933 in passing that β -NAT is apparently more prone to saturation than α -NAT. The Arrhenius
934 representation for the preferred TO results is:

$$935 \text{ TO Experiments: } \log J_{\text{ev}}(\text{H}_2\text{O})[\text{molec} \cdot \text{cm}^{-2} \cdot \text{s}^{-1}] = (36.0 \pm 1.3) - \frac{(77.0 \pm 4.9) \times 10^3}{2.303 RT} \quad (15)$$

936 HCl kinetic measurements on α -NAT and β -NAT indicate that HCl does not displace a
937 significant number of HNO_3 molecules from the ice surface upon deposition, but rather that
938 HCl and HNO_3 do not strongly interact with each other in the condensed phase and that HCl
939 evaporates faster. This observation is also supported by the slower rates of evaporation and
940 the correspondingly higher values of the HNO_3 evaporation activation energy on α -NAT and
941 β -NAT, $E_{\text{ev}}(\text{HNO}_3) = (178.0 \pm 27.4)$ and (102.0 ± 8.6) kJ mol^{-1} (see Table 4), respectively,

942 compared to the activation energy for HCl evaporation on HCl•6H₂O, $E_{\text{ev}}(\text{HCl}) = (87.0 \pm 17)$
 943 kJ mol⁻¹. This also is consistent with a larger calculated interaction energy of HNO₃ with H₂O
 944 (“affinity”) in α-NAT compared to β-NAT (Weiss et al., 2016) despite the fact that ΔH_f^0 (α-
 945 NAT) is less stable by 6.0 ± 20 kJ/mol compared to β-NAT.

946 A look at Table 5 reveals evaporative lifetimes of various ice particles with respect to H₂O
 947 evaporation. Equation (26) and (27) present the rudiments of a very simple layer-by-layer
 948 molecular model used to estimate evaporation lifetimes (θ_{tot}) at atmospheric conditions
 949 (Alcala et al., 2002; Chiesa and Rossi, 2013):

$$950 \quad \theta_{\text{tot}} = (r/a)N_{\text{ML}}/J_{\text{ev}}^{\text{rh}} \quad (26)$$

$$951 \quad J_{\text{ev}}^{\text{rh}} = J_{\text{ev}}^{\text{max}}(1-\text{rh}/100) \quad (27)$$

952 with r , a , rh and N_{ML} being the radius of the ice particle, shell thickness, relative humidity in
 953 % and the number of molecules cm⁻² corresponding to one monolayer. $J_{\text{ev}}^{\text{rh}}$ and $J_{\text{ev}}^{\text{max}}$ are the
 954 evaporation fluxes of H₂O at rh and $\text{rh} = 0$, the latter corresponding to the maximum value of
 955 J_{ev} which we calculate following Equation (2) or (8). The salient feature of this simple
 956 evaporation model is the linear rate of change of the radius or diameter of the particle, a well-
 957 and widely known fact in aerosol physics in which the shrinking or growing size (diameter) of
 958 an aerosol particle is linear with time if the rate of evaporation is zero order, that is
 959 independent of a concentration term.

960 Table 5 lists the evaporation life times which are not defined in terms of an e-folding time
 961 when dealing with first-order processes. In this example the lifetime is the time span between
 962 the cradle and death of the particle, this means from a given diameter $2r$ and “death” at $2r = 0$.
 963 The chosen atmospheric conditions correspond to 190 K, $\text{rh} = 80\%$, $a = 2.5 \text{ \AA}$ for H₂O and
 964 3.35 \AA for all other systems, $r = 10 \text{ \mu m}$ and estimated values 6×10^{14} , 3×10^{14} and 1×10^{15} molec
 965 cm⁻² for N_{ML} of HNO₃, HCl and H₂O. It is immediately apparent that there is a large variation
 966 of θ_{tot} values for atmospherically relevant conditions which goes into the direction of
 967 increasing opportunities for heterogeneous interaction with atmospheric trace gases, even for
 968 pure ice (PSC type II). Table 5 is concerned with the most volatile component, namely H₂O.

969 If we now turn our attention to the least volatile component such as HNO₃ in β-NAT we
 970 obtain $\theta_{\text{tot}} = 5.1 \text{ d}$ and 33.9 d for 0 and 85% HNO₃ atmospheric saturation, the former being
 971 the maximum possible evaporation rate for 0% HNO₃ saturation. The other boundary
 972 conditions are 190 K, polar upper tropospheric conditions at 11 km altitude (226.3 mb at 210

973 K), 1 ppb HNO₃, 10 ppm H₂O corresponding to 85% HNO₃ saturation. This goes to show that
974 laboratory experiments on gas-condensed phase exchange of lower volatility components in
975 atmospheric hydrates are fraught with complications. It follows as a corollary that both HCl,
976 but especially HNO₃ contamination of H₂O ice is bound to persist for all practical
977 atmospheric conditions.

978 At last it is useful to view the outcome of a recent laboratory experiment dealing with the
979 binary HNO₃/H₂O system monitored using a cryogenic mirror hygrometer (CMH) (Gao et al.,
980 2016) in light of the present kinetic results. In the basic experimental set-up the behavior of
981 the sample CMH exposed to a combined low pressure H₂O/HNO₃ flow is compared to the
982 response of a reference CMH that is located upstream of the HNO₃ source and exposed to the
983 H₂O flow alone, and has been described in detail by Thornberry et al. (2011). Any increase in
984 scattering of the incident monitoring laser beam owing to growth of the polycrystalline ice
985 deposit will be counterbalanced by heating of the mirror to bring back the optical detector
986 signal to a predetermined set point. The typical experimental sequence in Gao et al. (2016)
987 starts by establishing pure ice frost layers on both CMH mirrors at a stable mixing ratio of <
988 10 ppm after which a continuous flow of HNO₃ was added such that the flow past the sample
989 CMH contained 80-100 ppb HNO₃.

990 After typically one hour the gradual build-up of a NAT layer on the CMH was accompanied
991 by a temperature increase of the sample CMH to settle around the saturation temperature T_{sat}
992 of NAT at the chosen H₂O and HNO₃ flow rate. An increase of the H₂O flow from 6 to 80
993 ppm led to ice growth on both mirrors accompanied by an increase of T_{sat} of NAT adjusting to
994 the new H₂O flow rate. Suddenly, the HNO₃ flow was shut off which first led to a rapidly
995 decreasing MS signal for HNO₃ but ending up in an above background signal corresponding
996 to 0.5 to 1.0 ppb HNO₃. The temperature of the sample CMH continued to decrease below T_{sat}
997 of pure ice monitored by the reference CMH suggesting that $P_{\text{eq}}(\text{H}_2\text{O})$ of the condensate had
998 become larger than that of pure ice. This solid state on the sample CMH was called “second
999 condensate”. The low level of HNO₃ continued to react to repetitive increases (CMH heating)
1000 and decreases (CMH cooling) of the H₂O flow in a reproducible manner all the while staying
1001 below the level corresponding to T_{sat} of pure ice on the reference CMH. These repetitive H₂O
1002 on-off sequences provided additional evidence of the continued evaporation of HNO₃ from
1003 the condensate. The response of HNO₃ leaving the condensate undersaturated with respect to
1004 NAT is at first sight certainly unexpected based on the results displayed in Figures 2b and 4b.
1005 However, if one considers the relatively high mirror temperatures ranging between 207 and

1006 213 K between which the “second condensate” was cycled by way of changing the H₂O flows
1007 it suddenly becomes conceivable that $R_{\text{ev}}(\text{HNO}_3)$ becomes equal to $R_{\text{ev}}(\text{H}_2\text{O})$ in that
1008 temperature range. Linear extrapolation of the absolute rates of evaporation hints at similar
1009 magnitude for temperatures exceeding 210 K β - NAT (Figure 4). For α -NAT the temperature
1010 at which the evaporation rates of H₂O and HNO₃ become equal is even below 200 K owing to
1011 a steeper T-dependence of $R_{\text{ev}}(\text{HNO}_3)$ in α -NAT (Figure 2 and Table 4). We conclude, that
1012 the observed dynamics of the experiment performed by Gao et al. (2016) is entirely consistent
1013 with the kinetic results of the present study. However, the results of the Gao et al. (2016)
1014 laboratory experiment would certainly be different at lower temperatures more representative
1015 of the UT/LS.

1016

1017 **Acknowledgements**

1018 The authors would like to acknowledge the generous support of this work over the years by
1019 the Swiss National Science Foundation (SNSF) in the framework of projects 200020_125204
1020 and 200020_144431/1. We also sincerely thank Mr. Alwin Frei of PSI for graciously granting
1021 the permission to perform the experiments in his laboratory and professors Urs Baltensperger
1022 and Alexander Wokaun, both of PSI, for unfailing support over the years.

1023

1024 **References**

- 1025 Alcala-Jornod, A., van den Bergh, H., and Rossi, M.J.: Can soot particles emitted by airplane
1026 exhaust contribute to the formation of aviation contrails and cirrus clouds?, *Geophys. Res.*
1027 *Lett.* 29, 1820, doi:10.1029/2001GL014115, 2002.
- 1028 Benson, S.W., “Thermochemical Kinetics”, *Methods for the Estimation of Thermochemical*
1029 *Data and Rate Parameters*”, Second Edition, John Wiley and Sons, 1976.
- 1030 Berland, B.S., Haynes, D.R., Foster, K.L., Tolbert, M.A., George S.M. and Toon, O.B.:
1031 Refractive Indices of Amorphous and Crystalline HNO₃/H₂O Films Representative of Polar
1032 Stratospheric Clouds, *J. Phys. Chem.* 98, 4358-4364, 1994.
- 1033 Biermann, U. M., Crowley J.N., Huthwelker T., Moortgat G. K., Crutzen P. J., and Peter T.:
1034 FTIR studies on lifetime prolongation of stratospheric ice particles due to NAT coating,
1035 *Geophys. Res. Lett.*, 25(21), 3939–3942, 1998.
- 1036 Chaix, L., van den Bergh, H., and Rossi, M. J.: Real-Time kinetic measurements of the
1037 condensation and evaporation of D₂O molecules on ice at 140 K < T < 220 K, *J. Phys. Chem.*
1038 *A*, 102(50), 10300–10309, 1998.
- 1039 Crowley, J.N., Ammann, M., Cox, R.A., Hynes, R.G., Jenkin, M.E., Mellouki, A., Rossi,
1040 M.J., Troe, J., and Wallington, T.J.: Evaluated kinetic and photochemical data for
1041 atmospheric chemistry: Volume V – heterogeneous reactions on solid substrates, *Atmos.*
1042 *Chem. Phys.* 10, 9059-9223, 2010.
- 1043 Chiesa, S., and Rossi, M. J.: The metastable HCl•6H₂O phase – IR spectroscopy, phase
1044 transitions and kinetic/thermodynamic properties in the range 170-205 K, *Atmos. Chem.*
1045 *Phys.*, 13(23), 11905–11923, 2013; doi:10.5194/acp-13-11905-2013.
- 1046 Delval, C., Flückiger, B., and Rossi, M. J.: The rate of water vapor evaporation from ice
1047 substrates in the presence of HCl and HBr: implications for the lifetime of atmospheric ice
1048 particles, *Atmos. Chem. Phys.* 3, 1131–1145, 2003.
- 1049 Delval, C., and Rossi, M. J.: The kinetics of condensation and evaporation of H₂O from pure
1050 ice in the range 173-223 K: a quartz crystal microbalance study, *Phys. Chem. Chem. Phys.*, 6:
1051 4665–4676, 2004.

1052 Delval, C., and Rossi, M. J.: Influence of monolayer amounts of HNO₃ on the evaporation
1053 rate of H₂O over ice in the range 179 to 208 K: A quartz crystal microbalance study, *J. Phys.*
1054 *Chem. A*, 109(32), 7151–7165, 2005.

1055 Escribano, R. M., Fernandez-Torre, D., Herrero, V. J., Martin-Llorente, B., Maté, B., Ortega,
1056 I. K., and Grothe, H.: The low-frequency Raman and IR spectra of nitric acid hydrates, *Vib.*
1057 *Spectrosc.*, 43, 254–259, 2007.

1058 Fahey, D.W., Gao, R.S., Carslaw, K.S., Kettleborough, J., Popp, P.J., Northway, M.J.,
1059 Holecek, J.C., Ciciora, S.C., McLaughlin, R.J., Thompson, T.L., Winkler, R.H.,
1060 Baumgardner, D.G., Gandrud, B., Wennberg, P.O., Dhaniyala, S., McKinney, K., Peter, Th.,
1061 Salawitch, R.J., Bui, T.P., Elkins, J.W., Webster, C.R., Atlas, E.L., Jost, H., Wilson, J.C.,
1062 Herman, R.L., Kleinböhl, A., von König, M.: The Detection of Large HNO₃-Containing
1063 Particles in the Winter Arctic Stratosphere, *Science* 291, 1026-1031, 2001.

1064 Friedel, R. A., Shultz, J. L., and Sharkey, A. G.: Mass spectrum of nitric acid, *Anal. Chem.*,
1065 31(6), 1128–1128, 1959.

1066 Gao, R.S., Popp, P.J., Fahey, D.W., Marcy, T.P., Herman, R.L., Weinstock, E.M.,
1067 Baumgardner, D.G., Garrett, T.J., Rosenlof, K.H., Thompson, T.L., Bui, P.T., Ridley, B.A.,
1068 Wofsy, S.C., Toon, O.B., Tolbert, M.A., Kärcher, B., Peter, Th., Hudson, P.K., Weinheimer,
1069 A.J., Heymsfield, A.J.: Evidence That Nitric Acid Increases Relative Humidity in Low-
1070 Temperature Cirrus Clouds, *Science* 303, 516-520, 2004.

1071 Gao, R.S., Gierczak, T., Thornberry, T.D., Rollins, A.W., Burkholder, J.B., Telg, H., Voigt,
1072 C., Peter, T. and Fahey, D.W.: Persistent Water-Nitric Acid Condensate with Saturation
1073 Water Vapor Pressure Greater than That of Hexagonal Ice, *J. Phys. Chem. A* 120, 1431-1440,
1074 2016.

1075 Hamill, P., Turco, R. P., and Toon, O. B.: On the growth of nitric and sulfuric acid aerosol
1076 particles under stratospheric conditions. *J. Atmos. Chem.*, 7(3), 287–315, 1988.

1077 Hanson, D. R., and Mauersberger, K.: Laboratory studies of the nitric acid trihydrate:
1078 Implications for the south polar stratosphere, *Geophys. Res. Lett.*, 15(8), 855–858, 1988.

1079 Hanson, D. R.: The uptake of HNO₃ onto Ice, NAT and frozen sulfuric acid, *Geophys. Res.*
1080 *Lett.*, 19(20), 2063–2066, 1992.

1081 Herrero, V. J., Ortega, I. K., Maté, B., Martin-Llorente, B., Escribano, R., and H. Grothe:
1082 Comment on “Theoretical investigation of the coexistence of α - and β -nitric acid trihydrates

1083 (NAT) molecular conformation” [Chem. Phys. 324 (2006) 210], Chem. Phys., 331, 186–188,
1084 2006.

1085 Höpfner, M., Luo, B.P., Massoli, P., Cairo, F., Spang, R., Snels, M., Di Donfrancesco, G.,
1086 Stiller, G., von Clarmann, T., Fischer, H., Biermann, U.: Spectroscopic evidence for NAT,
1087 STS, and ice in the MIPAS infrared limb emission measurements of polar stratospheric
1088 clouds, Atmos. Chem. Phys., 6, 1201-1219, 2006.

1089 Hynes, R. G., Fernandez, M. A., and Cox, R. A.: Uptake of HNO₃ on water-ice and
1090 coadsorption of HNO₃ and HCl in the temperature range 210–235 K, J. Geophys. Res.
1091 Atmos., 107(D24), AAC 19–1–AAC 19–11, 2002.

1092 Iannarelli, R., and Rossi, M. J.: H₂O and HCl trace gas kinetics on crystalline HCl hydrates
1093 and amorphous HCl/H₂O in the range 170 to 205 K: the HCl/H₂O phase diagram revisited,
1094 Atmos. Chem. Phys., 14(10), 5183-5204, 2014.

1095 Iannarelli, R., and Rossi, M. J.: The mid-IR Absorption Cross Sections of α- and β-NAT
1096 (HNO₃•3H₂O) in the range 170 to 185 K and of metastable NAD (HNO₃•2H₂O) in the range
1097 172 to 182 K, J. Geophys. Res. Atmos., 120, 11707-11727, 2015.

1098 Ji, K. and Petit, J.-C., Calorimetric Identification of a new Nitric Acid Hydrate able to play a
1099 Role in the heterogeneous Chemistry of the Stratosphere, Compt. Rend. Acad. Sciences Ser
1100 II, 316(12), 1743-1748, 1993.

1101 Koehler, B. G., Middlebrook, A. M., and Tolbert, M. A.: Characterization of model polar
1102 stratospheric cloud films using Fourier transform infrared spectroscopy and temperature
1103 programmed desorption, J. Geophys. Res., 97(D8), 8065–8074, 1992.

1104 Kuhs, W. F., Sippel, C., Falenty, A., and Hansen, T. C.: Extent and relevance of stacking
1105 disorder in “ice I_c”, PNAS, 109(52), 21259– 21264, 2012.

1106 Marti, J., and Mauersberger, K.: A survey and new measurements of ice vapor pressure at
1107 temperatures between 170 and 250 K, Geophys. Res. Lett., 20, 363–366, 1993.

1108 Martin-Llorente, B., Fernandez-Torre, D., Herrero, V. J., Ortega, I. K., Escribano, R., and
1109 Maté, B.: Vibrational spectra of crystalline hydrates of atmospheric relevance: Bands of
1110 hydrated protons, Chem. Phys. Lett., 427, 300–304, 2006.

1111 Mauersberger, K., and Krankowsky, D.: Vapor pressure above ice at temperatures below 170
1112 K, Geophys. Res. Lett., 30(3), 1121, 2003.

1113 McElroy, M. B., Salawitch, R. J., and Wofsy, S. C.: Antarctic O₃: Chemical mechanisms for
1114 the spring decrease. *Geophys. Res. Lett.*, 13(12), 1296–1299, 1986.

1115 McNeill, V. F., Loerting, T., Geiger, F. M., Trout, B. L., and Molina, M. J.: Hydrogen
1116 chloride-induced surface disordering on ice. *PNAS*, 103(25), 9422–9427, 2006.

1117 McNeill, V. F., Geiger, F. M., Loerting, T., Trout, B. L., Molina, L. T., and Molina, M. J.:
1118 Interaction of hydrogen chloride with ice surfaces: the effects of grain size, surface roughness,
1119 and surface disorder. *J. Phys. Chem. A*, 111(28), 6274–6284, 2007.

1120 Middlebrook, A. M., Koehler, B. G., McNeill, L. S., and Tolbert, M. A.: Formation of model
1121 polar stratospheric cloud films, *Geophys. Res. Lett.*, 19(24), 2417–2420, 1992.

1122 Middlebrook, A.M., Tolbert, M.A., and Drdla, K.: Evaporation studies of model polar
1123 stratospheric cloud films, *Geophys. Res. Lett.* 23, 2145-2148, 1996.

1124 Molina, L. T., Molina M. J., Stachnik, R. A., and Tom, R. D.: An upper limit to the rate of the
1125 HCl + ClONO₂ reaction, *J. Phys. Chem.* 89, 3779-3781, 1985.

1126 Molina, M. J., Tso, T. L., Molina, L. T., and Wang, F. C. Y.: Antarctic stratospheric
1127 chemistry of chlorine nitrate, hydrogen chloride and ice: release of active chlorine, *Science*
1128 238, 1253-1257, 1987.

1129 Molina, M. J.: The Probable Role of Stratospheric ‘Ice’ Clouds: Heterogeneous Chemistry of
1130 the Ozone Hole, in “The Chemistry of the Atmosphere: Its Impact on Global Change”,
1131 Blackwell Scientific Publications, London, ch. 3, pp 27- 38, 1994.

1132 Moussa, S. G., Kuo, M. H., and McNeill, V. F.: Nitric acid-induced surface disordering on
1133 ice, *Phys. Chem. Chem. Phys.*, 15, 10989–10995, 2013.

1134 Ortega, I. K., Escribano, R., Fernandez, D., Herrero, V. J., Maté, B., Medialdea, A., and
1135 Moreno, M. A.: The structure and vibrational frequencies of crystalline nitric acid, *Chem.*
1136 *Phys. Lett.*, 378, 218–223, 2003.

1137 Ortega, I. K., Maté, B., Moreno, M. A., Herrero, V. J., and Escribano, R.: Infrared spectra of
1138 nitric acid trihydrate (β -NAT): A comparison of available optical constants and implication
1139 for the detection of polar stratospheric clouds (PSC’s), *Geophys. Res. Lett.*, 33 L19816, 2006.

1140 Peter, Th.: Microphysics and heterogeneous chemistry of Polar Stratospheric Clouds, *Annu.*
1141 *Rev. Phys. Chem.* 48, 785-822, 1997.

1142 Pratte P., van den Bergh H., and Rossi, M. J.: The kinetics of H₂O vapor condensation and
1143 evaporation on different types of ice in the range 130-210 K, *J. Phys. Chem A*, 110(9), 3042–
1144 3058, 2006.

1145 Reinhardt, H., Fida, M., and Zellner, R.: DRIFTS-studies of the interactions of HNO₃ with ice
1146 and HCl (HNO₃)-hydrate surfaces at temperatures around 165 K, *J. Mol. Struct.*, 661–662,
1147 567–577, 2003.

1148 Ritzhaupt, G., and Devlin, J. P.: Infrared spectra of nitric and hydrochloric acid hydrate thin
1149 films, *J. Phys. Chem.* 95, 90-95, 1991.

1150 Schreiner, J., Voigt, C., Kohlmann, A., Arnold F., Mauersberger, K. and Larsen, Niels,
1151 *Chemical Analysis of Polar Stratospheric Cloud Particles*, *Science*, 283, 968-970, 1999.

1152 Schreiner, J., Voigt, C., Weisser, C., Kohlmann, A., Mauersberger, K., Deshler, T., Kröger,
1153 C., Rosen, J., Kjöme, N., Larsen, N., Adriani, A., Cairo, F., Di Donfrancesco, G., Ovarlez, J.,
1154 Ovarlez, H., and Dörnbrack, A.: Chemical, microphysical, and optical properties of polar
1155 stratospheric clouds, *J. Geophys. Res.*, 108(D5), 8313, 2003.

1156 Solomon, S., Garcia, R.R., Rowland, F.S., and Wuebbles, D.J.: On the depletion of Antarctic
1157 ozone, *Nature* 321, 755-758, 1986.

1158 Solomon, S.: Progress towards a quantitative understanding of Antarctic ozone depletion,
1159 *Nature* 347, 347-354, 1990.

1160 Thornberry, T.D., Gierczak, T., Gao, R.S., Vömel, H., Watts, L.A., Burkholder, J.B., Fahey,
1161 D.W.: Laboratory evaluation of the effect of nitric acid uptake on frost point hygrometer
1162 performance, *Atmos. Meas. Tech.* 4, 289-296, 2011.

1163 Tolbert, M. A., and Middlebrook, A. M.: Fourier transform infrared studies of model polar
1164 stratospheric cloud surfaces: Growth and evaporation of ice and nitric acid/ice, *J. Geophys.*
1165 *Res.*, 95(D13), 22423–22431, 1990.

1166 Tolbert, M. A., Koehler, B. G., and Middlebrook, A. M.: Spectroscopic studies of model polar
1167 stratospheric cloud films, *Spectrochim. Acta Part A: Mol. Spectrosc.*, 48(9), 1303–1313,
1168 1992.

1169 Toon, O.B., Tolbert, M.A., Koehler, B.G., Middlebrook, A.M. and J. Jordan, J.: Infrared
1170 optical constants of H₂O ice, amorphous nitric acid solutions, and nitric acid hydrates,
1171 *Geophys. Res.* 99(D12), 25631-25654 (1994).

1172 Tso, T.-L., and Leu, M.-T.: Quantitative analysis of the infrared absorptivities of nitric acid
1173 ices existing in polar stratospheric clouds, *Anal. Sci.*, 12, 615–622, 1996.

1174 Voigt, C., Schreiner, J., Kohlmann, A., Zink, P., Mauersberger, K., Larsen, N., Deshler, T.,
1175 Kröger, C., Rosen, J., Adriani, A., Cairo, F., Di Donfrancesco, G., Viterbini, M., Ovarlez, J.,
1176 Ovarlez, H., David, C., and Dörnbrack A.: Nitric Acid Trihydrate (NAT) in Polar
1177 Stratospheric Clouds, *Science*, 290, 1756-1758, 2000.

1178 Voigt, C., Schreiner, J., Kohlmann, A., Zink, P., Mauersberger, K., Larsen, N., Deshler, T.,
1179 Kröger, C., Rosen, J., Adriani, A., Cairo, F., Di Donfrancesco, G., Viterbini, M., Ovarlez, J.,
1180 Ovarlez, H., David, C. and Dörnbrack, A., *Science* 290, 1756-1758, 2000.

1181 Voigt, C., Schlager, H., Luo, B.P., Dörnbrack, A., Roiger, A., Stock, P., Curtius, J., Vössing,
1182 H., Borrmann, S., Davies, S., Konopka, P., Schiller, C., Shur, G. and Peter, T.: Nitric Acid
1183 Trihydrate (NAT) formation at low NAT supersaturation in Polar Stratospheric Clouds
1184 (PSC's), *Atmos. Chem. Phys.*, 5, 1371-1380, 2005.

1185 Warshawsky, M.S., Zondlo, M.A., and Tolbert, M.A.: Impact of nitric acid on ice evaporation
1186 rates, *Geophys. Res. Lett.* 26, 823-826, 1999.

1187 Weiss, F., Kubel, F., Gálvez, O., Hoelzel, M., Parker, S. F., Baloh, P., Iannarelli, R., Rossi,
1188 M. J., and Grothe, H.: Metastable Nitric Acid Trihydrate in Ice Clouds, *Angew. Chemie I.E.*
1189 55, 3276-3280, 2016, doi: 10.1002/anie.201510841.

1190 Wooldridge, P. J., Zhang, R., and Molina, M. J.: Phase equilibria of H₂SO₄, HNO₃, and HCl
1191 hydrates and the composition of polar stratospheric clouds, *J. Geophys. Res. Atmos.*,
1192 100(D1), 1389–1396, 1995.

1193 Zondlo, M. A., Barone, S. B., and Tolbert, M. A.: Condensed-phase products in
1194 heterogeneous reactions: N₂O₅, ClONO₂, and HNO₃ reacting on ice films at 185 K, *J. Phys.*
1195 *Chem. A*, 102, 5735–5748, 1998.

1196 Zondlo, M.A., Hudson, P.K., Prenni, A.J., and Tolbert, M.A.: Chemistry and microphysics of
1197 polar stratospheric clouds and cirrus clouds, *Ann. Rev. Phys. Chem.* 51, 473-499, 2000.
1198

1199 Table 1: Characteristic parameters of the used Stirred Flow Reactor (SFR).

Reactor volume (upper chamber)	$V_R = 2036 \text{ cm}^3$		
MS (lower) chamber	$V_{MS} = 1750 \text{ cm}^3$		
Reactor internal surface	$S_W = 1885 \text{ cm}^2$		
H ₂ O calibrated volume – inlet line	$V_{\text{water}} = 62 \text{ cm}^3$		
HNO ₃ calibrated volume – inlet line	$V_{\text{acid}} = 20 \text{ cm}^3$		
Si support area (one side)	$A_{Si} = 0.99 \text{ cm}^2$		
Surface to Volume ratio	$2 A_{Si}/V_R = 0.9725 \times 10^{-4} \text{ cm}^{-1}$		
Reactor wall temperature	$T_w = 315 \text{ K}$		
Conversion of evaporation rate and flux	$R_{ev} \cdot V_R = 2 \cdot A_{Si} \cdot J_{ev}$		
	HNO₃	H₂O	HCl
Base Peak Signal MS [m/z]	46	18	36
MS Calibration Factor C^X [molec ⁻¹ s A]	4.53×10^{-25}	6.65×10^{-25}	1.30×10^{-25}
Escape rate constant			
$k_{esc}^S = C^S \sqrt{\frac{T}{M}}$ (small orifice) [s ⁻¹]	0.0913	0.1710	0.1213
$k_{esc}^M = C^M \sqrt{\frac{T}{M}}$ (both orifices) [s ⁻¹]	0.4331	0.8102	0.5729
Gas-surface collision frequency at 315 K, one side [s ⁻¹] ^(a) $\omega = \frac{\bar{c}}{4V} \cdot A_{Si} = \sqrt{\frac{8RT}{\pi M}} \cdot \frac{A_{Si}}{4V}$	3.95	7.39	5.22

1200 ^(a) M in kg; A_{Si} in m²; V in m³; R = 8.314 J K⁻¹ mol⁻¹. “One side” corresponds to front or rear side of Si-window.
 1201 In order to calculate the accommodation coefficient α using equation (3) we have used 2ω as the total collision
 1202 frequency for both sides of the Si-window.
 1203

1204 Table 2: Fit parameters of the Langmuir adsorption isotherms for H₂O, HNO₃ and HCl
 1205 interaction with the internal stainless steel (SS304) surfaces of the SFR.

Adsorbed Gas (Additional Gas) ^(a)	K_L [×10 ⁻¹⁴] ^(b)	N_{TOT} [×10 ¹⁷] ^(c)	N_{MAX} [×10 ¹⁴] ^(d)	α_w [×10 ⁻⁶] ^(e)
H ₂ O	3.18 ± 0.38	7.03 ± 0.42	3.73 ± 0.22	6.19 ± 0.08
H ₂ O (HCl, F _{in} = 8×10 ¹⁴)	4.67 ± 0.39	8.38 ± 0.29	4.45 ± 0.15	—
HNO ₃	1.10 ± 0.16	93 ± 11	49 ± 6	2.92 ± 0.10
HNO ₃ (H ₂ O, F _{in} = 2-3×10 ¹⁵)	1.61 ± 0.40	76 ± 15	40 ± 8	—
HNO ₃ (average values)	1.28 ± 0.17	84 ± 8	45 ± 4	—
HCl	437 ± 21	5.06 ± 0.06	2.68 ± 0.03	16.9 ± 0.3
HCl (H ₂ O, F _{in} = 6×10 ¹⁵)	63.1 ± 4.9	4.85 ± 0.07	2.57 ± 0.04	—
HCl (H ₂ O, F _{in} = 3×10 ¹⁵)	64.6 ± 6.3	3.79 ± 0.09	2.01 ± 0.04	—

1206 ^(a) F_{in} is the flow rate of the additional gas in molec s⁻¹.

1207 ^(b) K_L is the Langmuir adsorption equilibrium constant in cm³ molec⁻¹.

1208 ^(c) N_{TOT} is the total number of adsorbed molecules onto the internal surfaces, reported is the saturation value for
 1209 total internal surface (1885 cm²) of SFR.

1210 ^(d) N_{MAX} is the adsorption site density in molec cm⁻².

1211 ^(e) α_w is the reactor wall accommodation coefficient.

1212

1213

1214 Table 3: Peak Positions in cm^{-1} in the mid-IR of HNO_3 and HNO_3/HCl Hydrates^a.

α -NAT/HCl this work	β -NAT/HCl this work	α -NAT/ice Iannarelli et al., 2015	β -NAT/ice Iannarelli et al., 2015	HCl/H ₂ O am Iannarelli et al., 2014
3430 (sh)		3430		
3354 (sh)	3360		3377	3360
3233 ^b	3227 ^b	3233 ^b	3233 ^b	3236 ^b
1767 ^{c,d}	1850 ^c	1760 ^c	1850 ^c	1730 ^c
1828 ^{c,d} , 1625-1560 ^{c,d}				1639 ^c
1375	1378	1385	1378	
1328	1339		1339	
1196	1198			

1215 ^a Values in italics indicate significant changes in the spectrum upon addition of HCl to α - or β -NAT.1216 ^b The vibration on the third entry invariably corresponds to ν_3 (antisymmetric stretch) H-O-H in H₂O ice.1217 ^c Broad band. The estimated uncertainty in the peak position is ± 7.5 compared to the usual $\pm 2 \text{ cm}^{-1}$.1218 ^d With increasing HCl content broad band at 1767 cm^{-1} splits into two bands at 1828 and $1525\text{-}1650 \text{ cm}^{-1}$.

1219

1220

1221

1222

1223

1224

1225 Table 4: Synopsis of thermodynamic (P_{eq}) and kinetic (J_{ev}) parameters of the Arrhenius and
 1226 van 't Hoff representation of data from Figure 2, Figure 4, Figure 8 and Figure 9.

			$J_{\text{ev}}^{(a)}$		$P_{\text{eq}}^{(b)}$	
			E_{ev}	A	ΔH_{ev}^0	$\Delta S/R$
Sample	Gas	Exp.				
α -NAT	H ₂ O	TO	75.3 ± 9.9	35.9 ± 2.8	70.3 ± 14.1	15.2 ± 4.0
		PV	3.5 ± 4.2	15.1 ± 1.2	56.5 ± 5.1	11.8 ± 1.5
	HNO ₃	TO	178.0 ± 27.4	62.3 ± 7.8	128.6 ± 42.4	29.3 ± 12.0
	HCl	PV	78.3 ± 19.2	34.8 ± 5.3	78.4 ± 11.4	15.7 ± 3.2
β -NAT	H ₂ O	TO	77.0 ± 4.9	36.0 ± 1.3	76.7 ± 17.7	16.7 ± 4.9
		PV	52.1 ± 2.4	28.7 ± 0.7	75.5 ± 11.1	16.7 ± 3.0
	HNO ₃	TO	102.0 ± 8.6	40.6 ± 2.4	96.5 ± 12.0	19.8 ± 3.3
	HCl	PV	56.7 ± 4.6	28.6 ± 1.3	69.6 ± 5.8	13.3 ± 1.6

1227 ^(a) for gas X, $R = 8.314 \text{ J K}^{-1} \text{ mol}^{-1}$: $\log J_{\text{ev}}(\text{X})[\text{molec} \cdot \text{cm}^{-2} \cdot \text{s}^{-1}] = A - \frac{E_{\text{ev}} \times 10^3}{2.303 RT}$

1228 ^(b) for gas X, $R = 8.314 \text{ J K}^{-1} \text{ mol}^{-1}$: $\log P_{\text{eq}}(\text{X})[\text{Torr}] = \frac{\Delta S}{R} - \frac{\Delta H_{\text{ev}}^0 \times 10^3}{2.303 RT}$

1229

1230

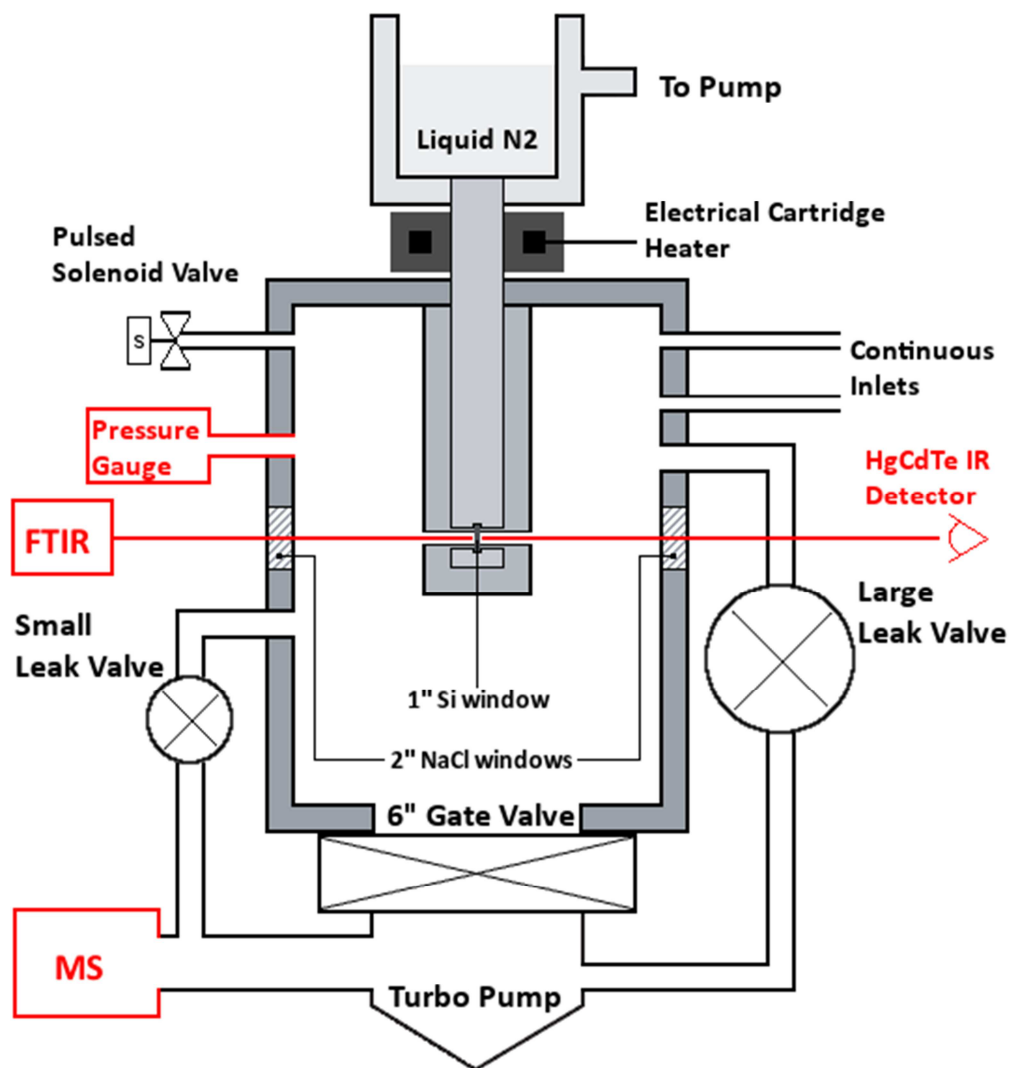
1231 Table 5: Atmospheric Lifetimes of various 20 μm diameter Ice Particles at 190 K calculated
 1232 using the measured absolute rate of H_2O evaporation of corresponding ice particle^a

Molecular System	Evaporation Flux $J_{\text{ev}}(\text{M})$ (molecule $\text{cm}^{-2} \text{s}^{-1}$)	Lifetime θ/h	Dopant Dose/ML (molecular monolayer)
H_2O	2.1×10^{16}	2.6	pure
$\text{HCl}/\text{H}_2\text{O}$	5.1×10^{15}	10.9	< 3 ML
	1.4×10^{15}	39.7	23 ML
$\text{HBr}/\text{H}_2\text{O}$	2.1×10^{15}	26.5	< 3 ML
$\alpha\text{-NAT}/\text{H}_2\text{O}$	1.8×10^{15}	23.1	pure
$\beta\text{-NAT}/\text{H}_2\text{O}$	6.0×10^{14}	69.4	pure

1233 ^a Conditions: $T = 190 \text{ K}$, $\text{rh} = 80\%$, a corresponds to experimentally measured interlayer distance (XRD), $a = 2.5$
 1234 and 3.35 \AA for H_2O , HCl -, HBr - H_2O and NAT , resp., $r = 10 \mu\text{m}$ ice particle, ML for HNO_3 , HCl , H_2O is 6×10^{14} ,
 1235 3×10^{14} , 1×10^{15} , respectively.

1236

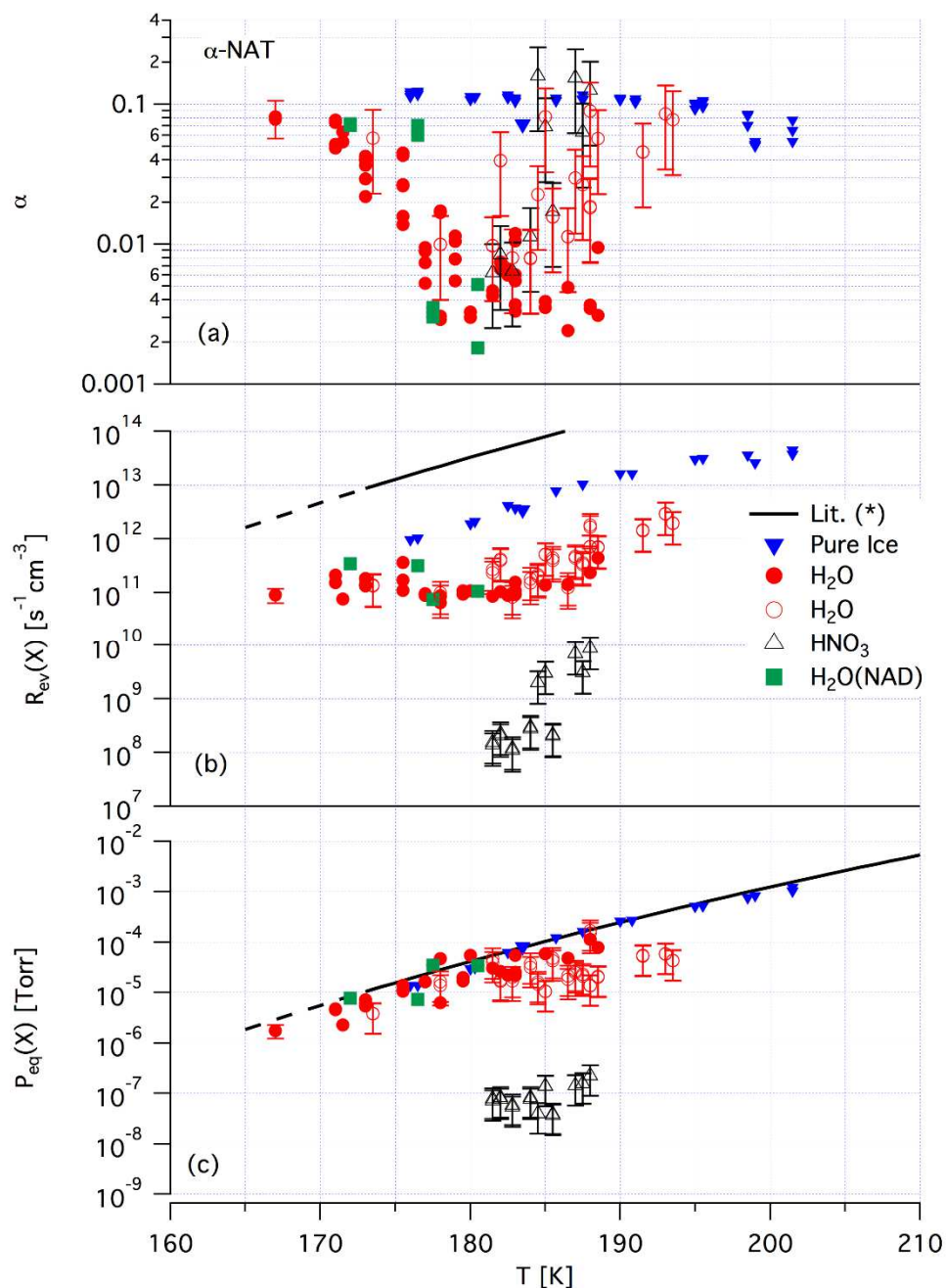
1237



1238

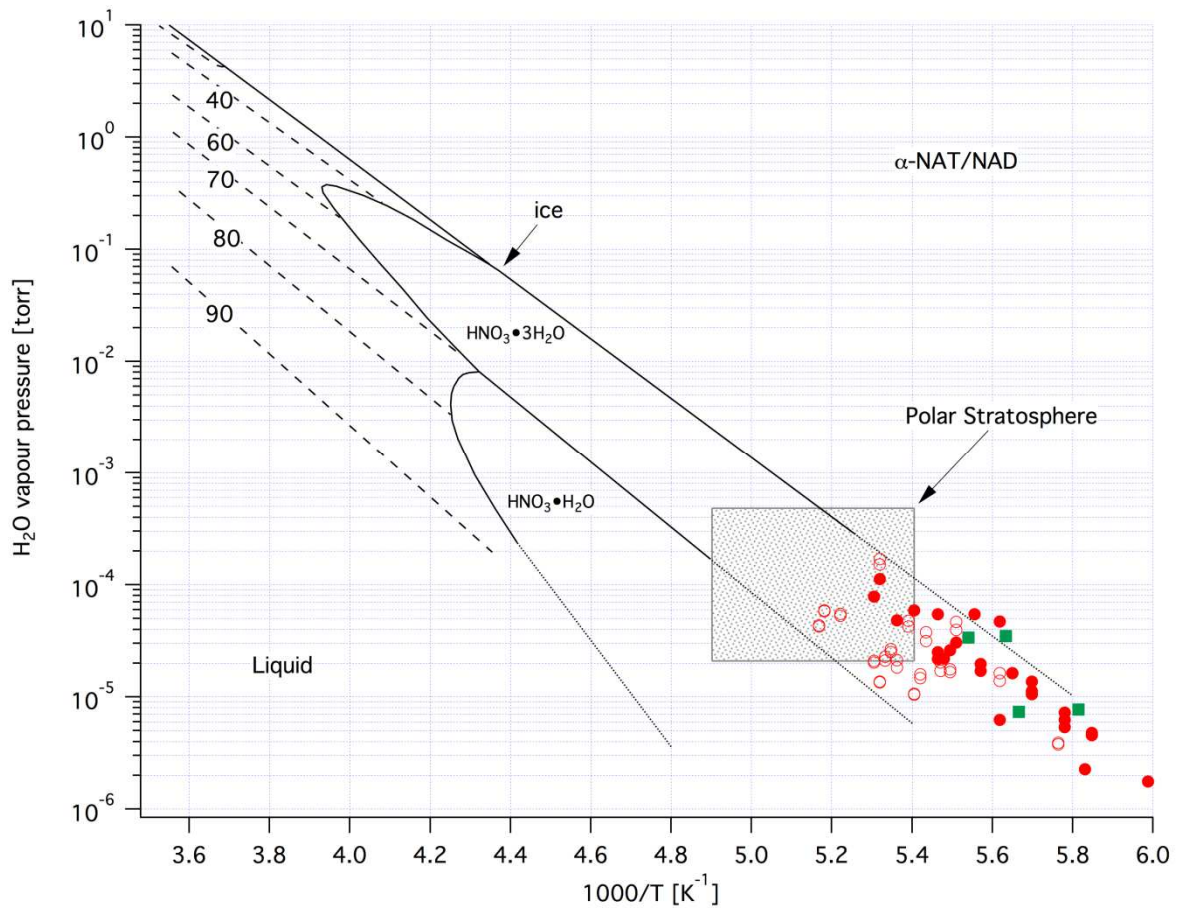
1239 Figure 1: Schematic drawing of the reactor used in this work. The diagnostic tools are
 1240 highlighted in red and important parameters are listed in Table 1 and Table 2. The ice film is
 1241 deposited on both sides of the 1" diameter Si window (black vertical symbol hanging from
 1242 cryostat inside reaction vessel).

1243



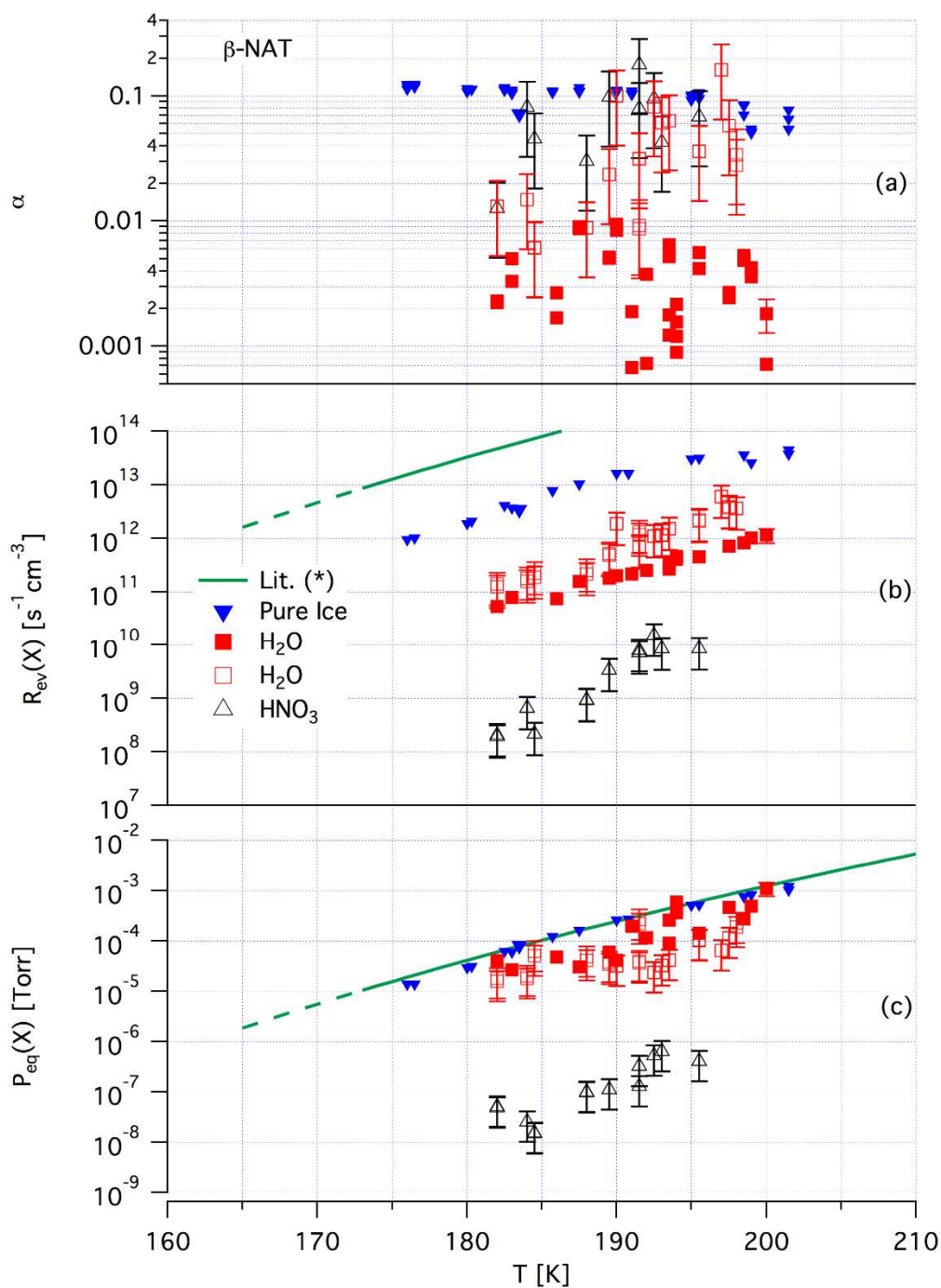
1244

1245 Figure 2: Synopsis of kinetic results for α -NAT and NAD using H_2O as a probe gas in PV
 1246 experiments and H_2O and HNO_3 in two-orifice (TO) experiments. Full symbols represent PV
 1247 experiments and empty symbols represent TO experiments. The different symbols are coded
 1248 in panel b. The calculated relative error for PV experiments is 30% whereas for TO
 1249 experiments we estimate a relative error of 60%. Examples of the amplitude of the errors are
 1250 reported for selected points. The black line shows results from Marti and Mauersberger
 1251 (1993) with $R_{\text{ev}}(\text{H}_2\text{O})$ of pure ice calculated for the system in use using $\alpha = 1$.



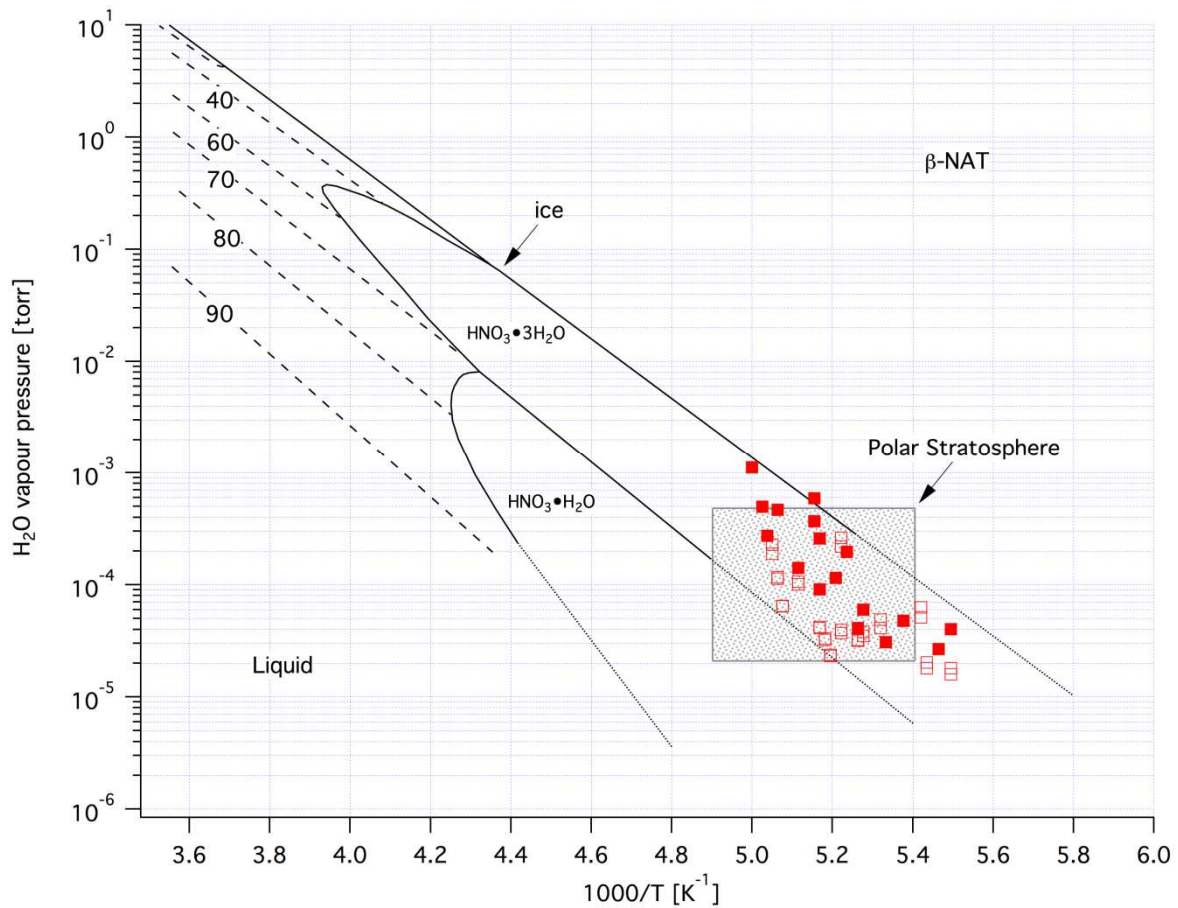
1252

1253 Figure 3: Binary phase diagram of the $\text{HNO}_3/\text{H}_2\text{O}$ system reconstructed from McElroy et al.
 1254 (1986); Hamill et al. (1988); Molina (1994). The full symbols represent calculated values of
 1255 $P_{\text{eq}}(\text{H}_2\text{O})$ for $\alpha\text{-NAT}$ and NAD using the kinetic data of PV experiments. Empty circles
 1256 represent calculated values of $P_{\text{eq}}(\text{H}_2\text{O})$ for $\alpha\text{-NAT}$ using the kinetic data of two-orifice (TO)
 1257 experiments. The solid lines represent the coexistence conditions for two phases and the
 1258 dashed lines represent vapor pressures of liquids with composition given as % (w/w) of
 1259 HNO_3 . The shaded gray represents polar stratospheric conditions.



1260

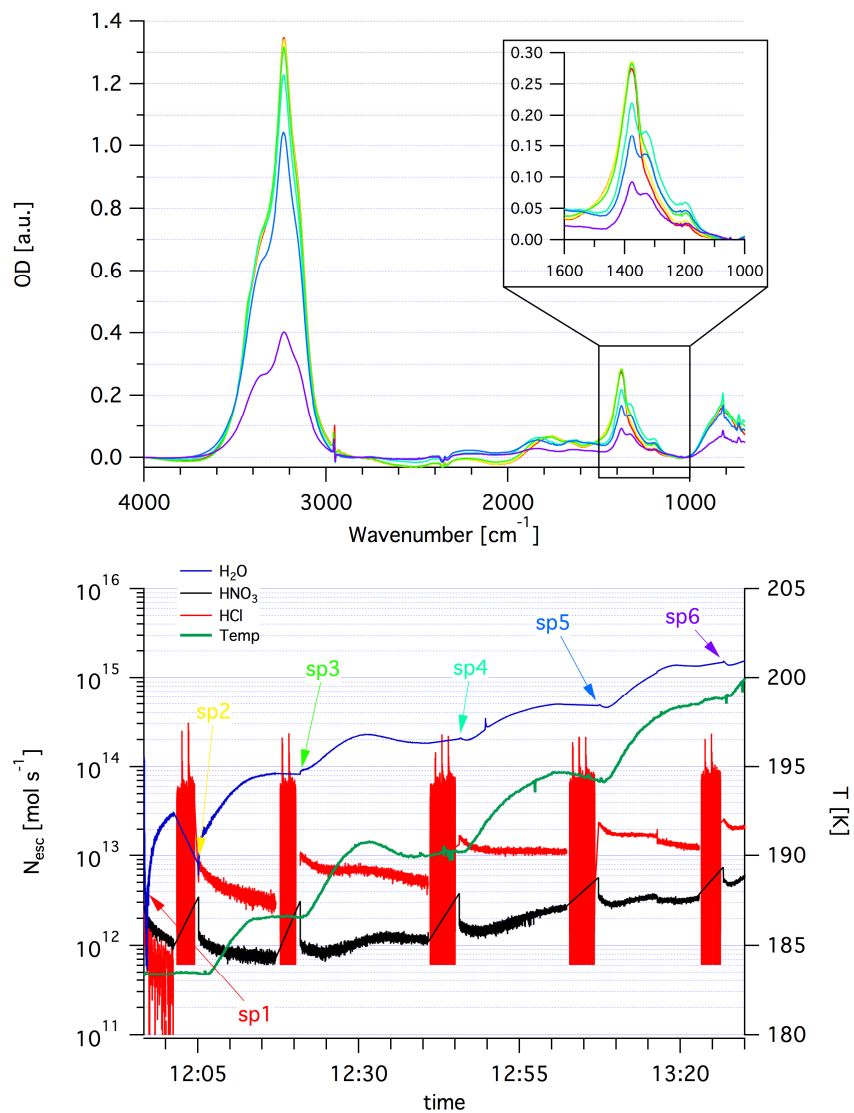
1261 Figure 4: Synopsis of kinetic results for β -NAT using H_2O as a probe gas in PV experiments
 1262 and H_2O and HNO_3 in two-orifice experiments. Full symbols represent PV experiments and
 1263 empty symbols represent TO experiments. The different symbols are coded in panel b. The
 1264 calculated relative error for PV experiments is 30% whereas for TO experiments we estimate
 1265 a relative error of 60%. Examples of the amplitude of the errors are reported for selected
 1266 points. The green line shows results from Marti and Mauersberger (1993).



1267

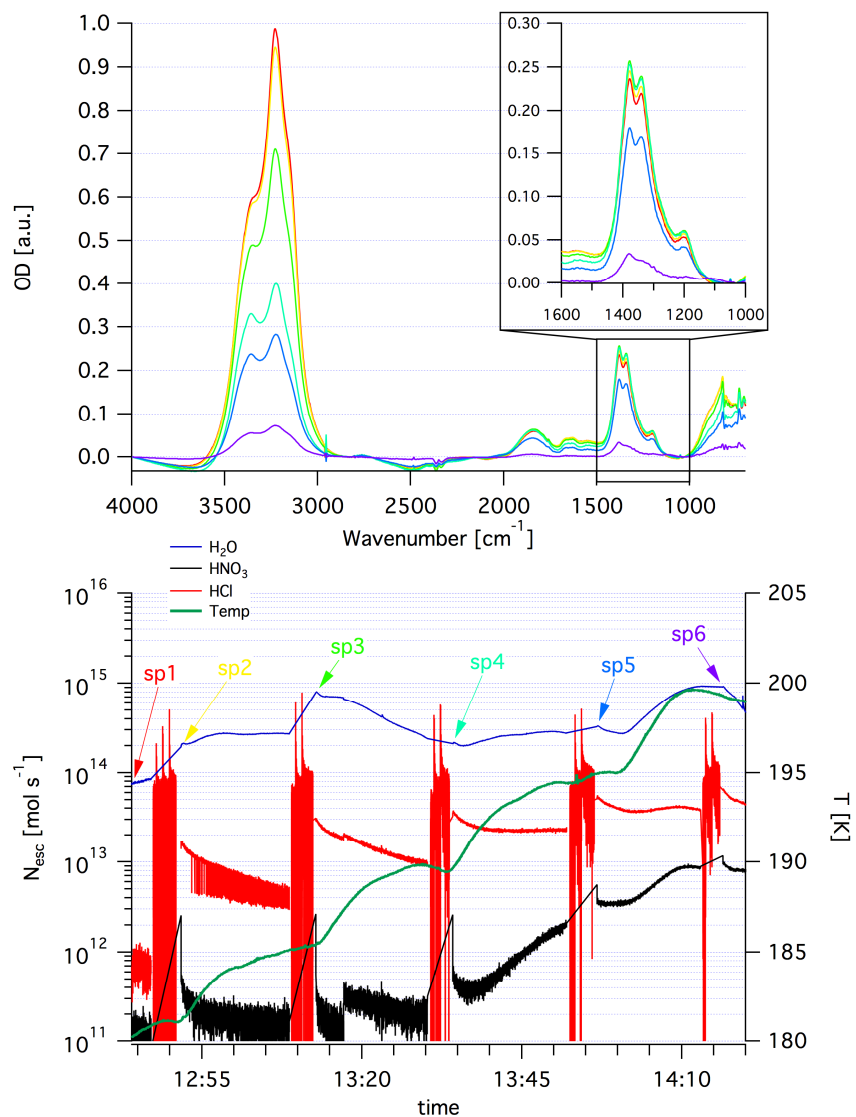
1268 Figure 5: Binary phase diagram of the $\text{HNO}_3/\text{H}_2\text{O}$ system reconstructed from McElroy et al.
 1269 (1986); Hamill et al. (1988); Molina (1994). The full symbols represent calculated values of
 1270 $P_{\text{eq}}(\text{H}_2\text{O})$ for $\beta\text{-NAT}$ using the kinetic data of PV experiments. Empty circles represent
 1271 calculated values of $P_{\text{eq}}(\text{H}_2\text{O})$ using the kinetic data of TO (Two-Orifice) experiments. The
 1272 solid lines represent the coexistence conditions for two phases and the dashed lines represent
 1273 vapor pressures of liquids with composition given as % (w/w) of HNO_3 . The shaded gray
 1274 represents polar stratospheric conditions.

1275



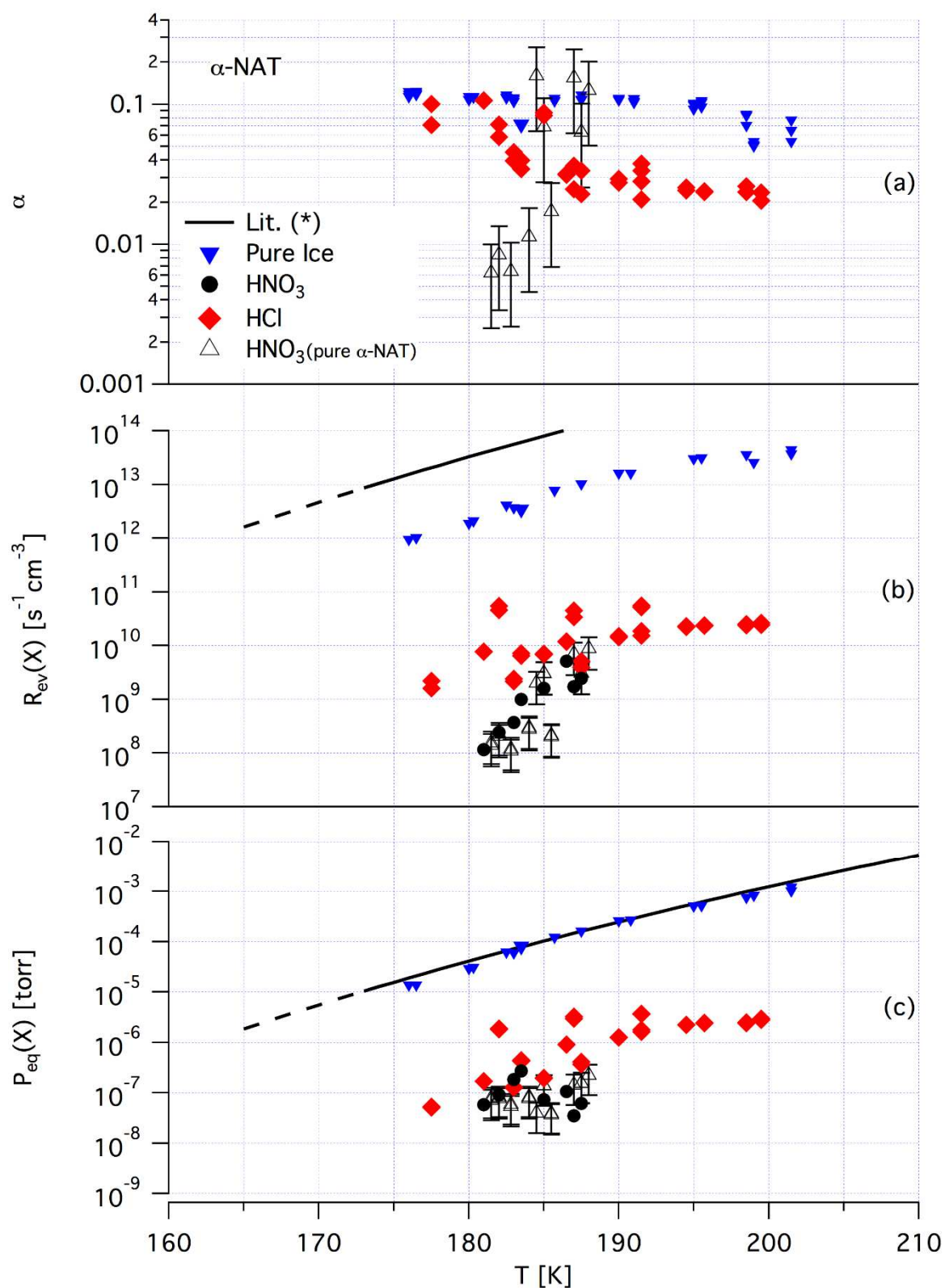
1276

1277 Figure 6: Repetitive PV (Pulsed Valve) deposition experiment of HCl on an α -NAT/ice
 1278 substrate under SFR conditions followed by MS (lower panel) and FTIR transmission across
 1279 the thin film (upper panel) as a function of time. In the lower panel the temperature is
 1280 displayed as the green trace, the red MS signal represents HCl at m/e 36 amu with the pulsed
 1281 forcing recognizable as single peaks (12) on top of the red columns. The individual HCl doses
 1282 correspond to approximately $(4-5) \times 10^{16}$ molecule per pulse resulting in a total dose of 3×10^{17}
 1283 molecules. The blue and black traces represent the response of H_2O (m/e 18 amu) and HNO_3
 1284 (m/e 46 amu) as a function of time (temperature) and HCl forcing. The upper trace displays
 1285 FTIR transmission spectra at selected times indicated in the lower panel through color coding.
 1286 The principal peak positions are listed in Table 3 and the changes are discussed in the text.
 1287



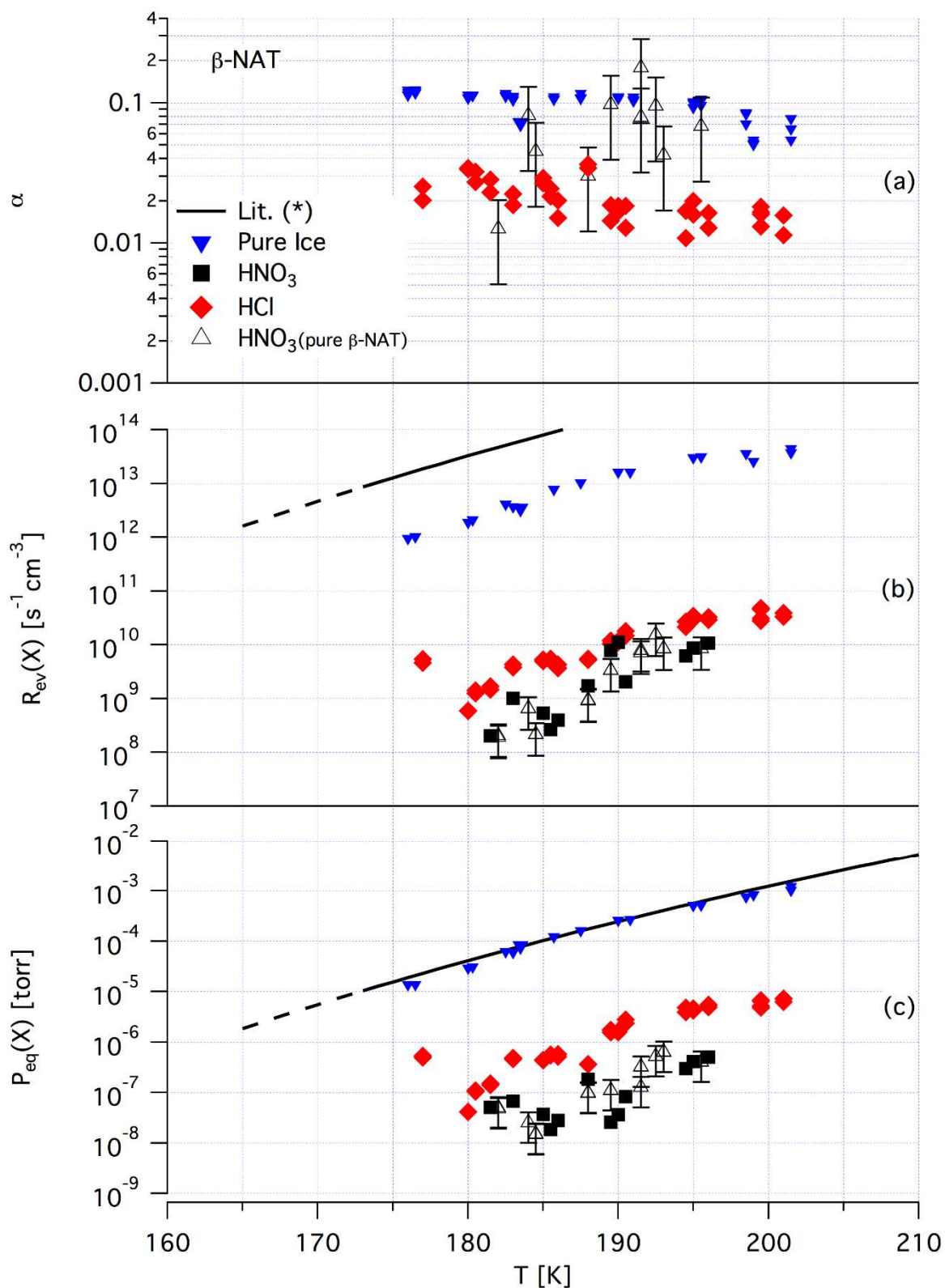
1288

1289 Figure 7: Repetitive PV (Pulsed Valve) deposition experiment of HCl on an β -NAT/ice
 1290 substrate under SFR conditions followed by MS (lower panel) and FTIR transmission across
 1291 the thin film (upper panel) as a function of time. In the lower panel the temperature is
 1292 displayed as the green trace, the red MS signal represents HCl at m/e 36 amu with the pulsed
 1293 forcing recognizable as single peaks (11) on top of the red columns. The individual HCl doses
 1294 correspond to approximately $(6-7) \times 10^{16}$ molecule per pulse resulting in a total dose of 4×10^{17}
 1295 molecules. The blue and black traces represent the response of H_2O (m/e 18 amu) and HNO_3
 1296 (m/e 46 amu) as a function of time (temperature) and HCl forcing. The upper trace displays
 1297 FTIR transmission spectra at selected times indicated in the lower panel through color coding.
 1298 The principal peak positions are listed in Table 3 and the changes are discussed in the text.
 1299



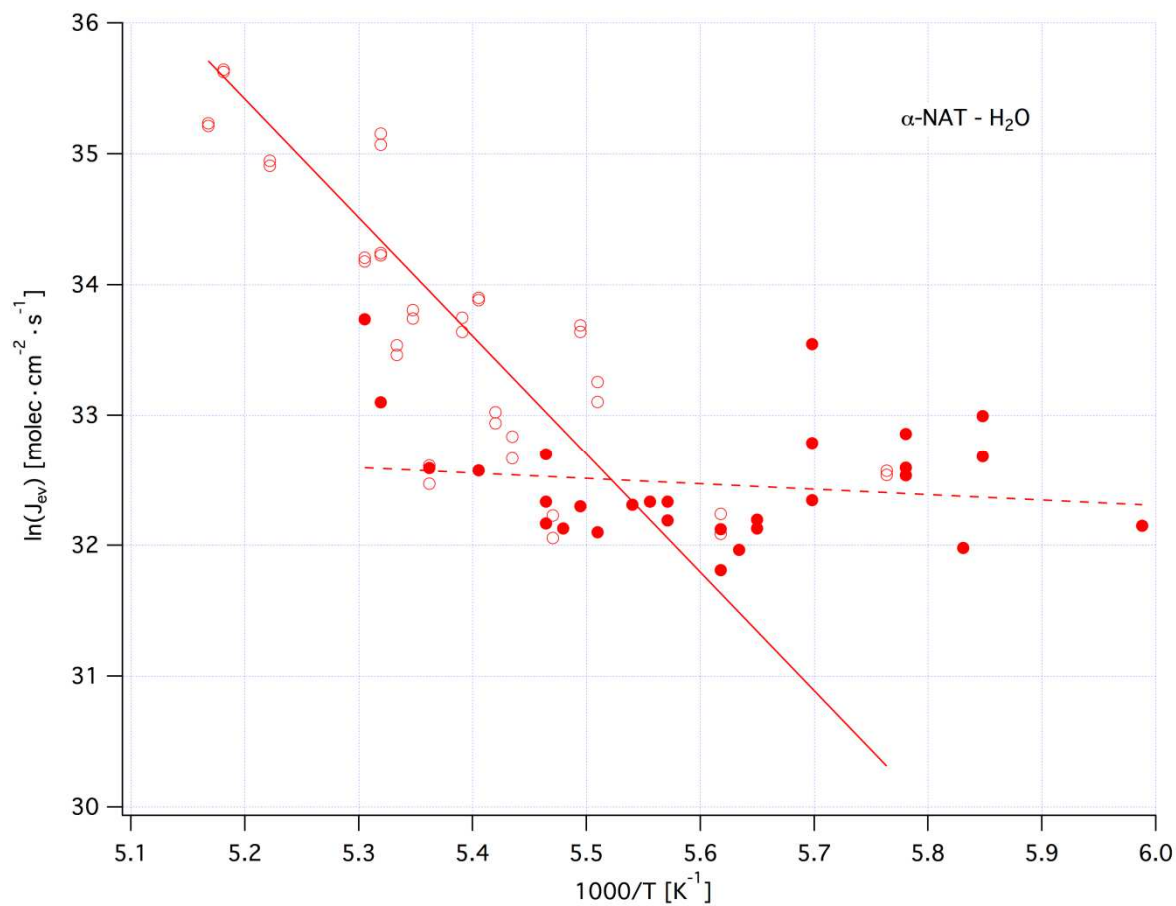
1300

1301 Figure 8: Synopsis of kinetic results for α -NAT using HCl as a probe gas in PV experiments.
 1302 The used symbols are coded in the upper panel. The calculated relative error for PV
 1303 experiments is 30%. The black line shows results from Marti and Mauersberger (1993).



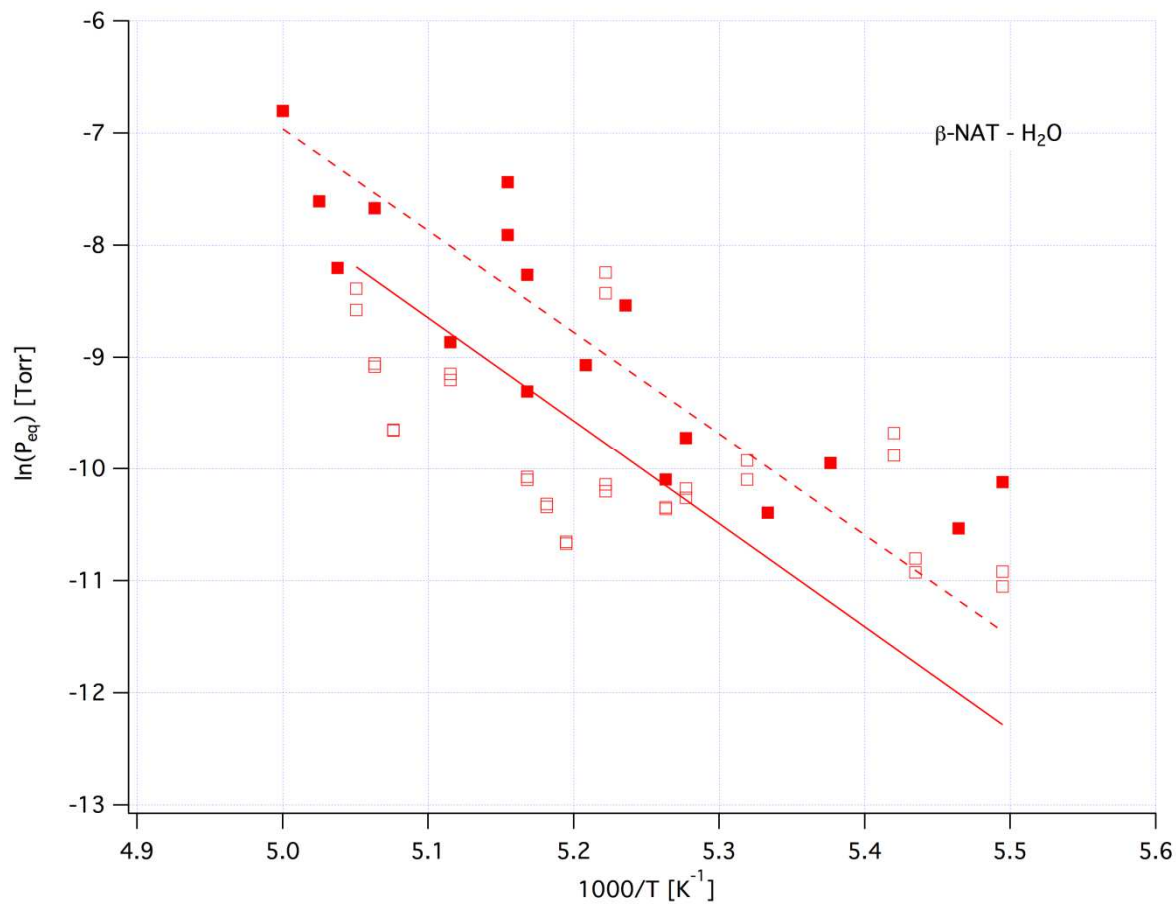
1304

1305 Figure 9: Synopsis of kinetic results for β -NAT using HCl as a probe gas in PV experiments.
 1306 The used symbols are coded in the upper panel. The calculated relative error for PV
 1307 experiments is 30%. The black line shows results from Marti and Mauersberger (1993).



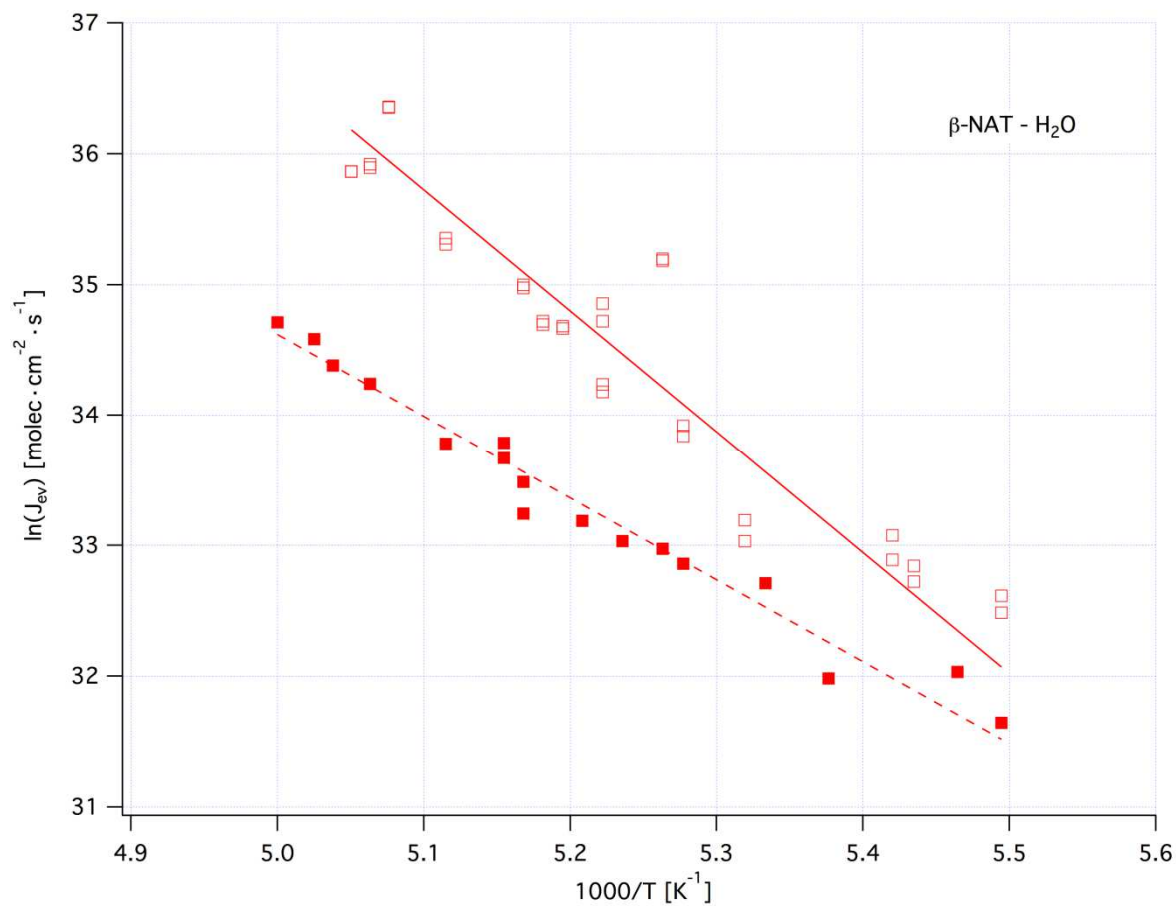
1308

1309 Figure 10: Arrhenius plot of $J_{ev}(\text{H}_2\text{O})$ for α -NAT. Full and empty red circles represent results
 1310 of PV and TO experiments, respectively. Data are taken from Figure 2b and the equations for
 1311 the linear fits may be found in the text.



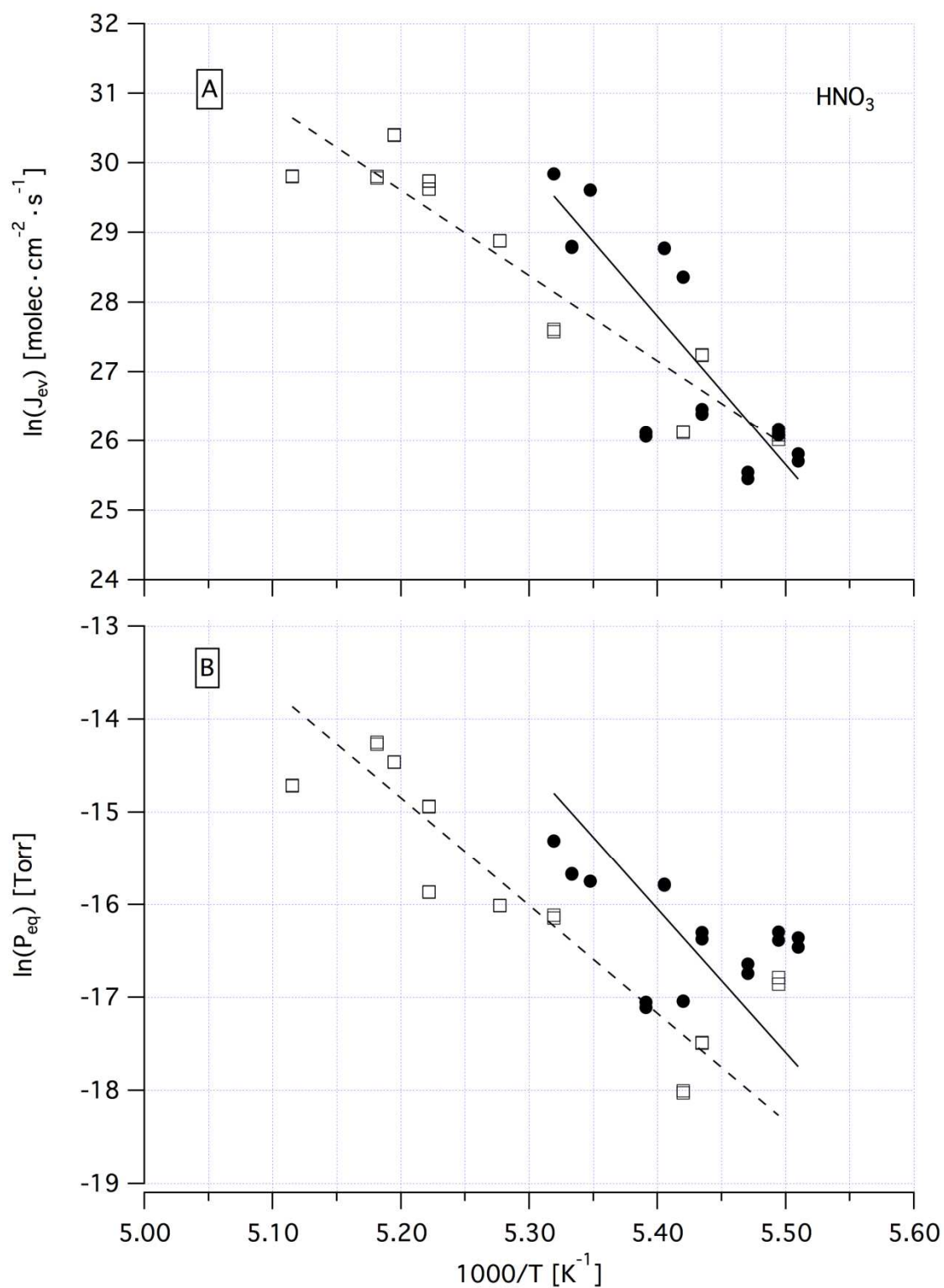
1312

1313 Figure 11: van 't Hoff plot of $P_{eq}(H_2O)$ for β -NAT data displayed in Figure 4c. Full and
1314 empty red squares represent results of PV and TO experiments, respectively. The equations
1315 for the linear fits may be found in the text.



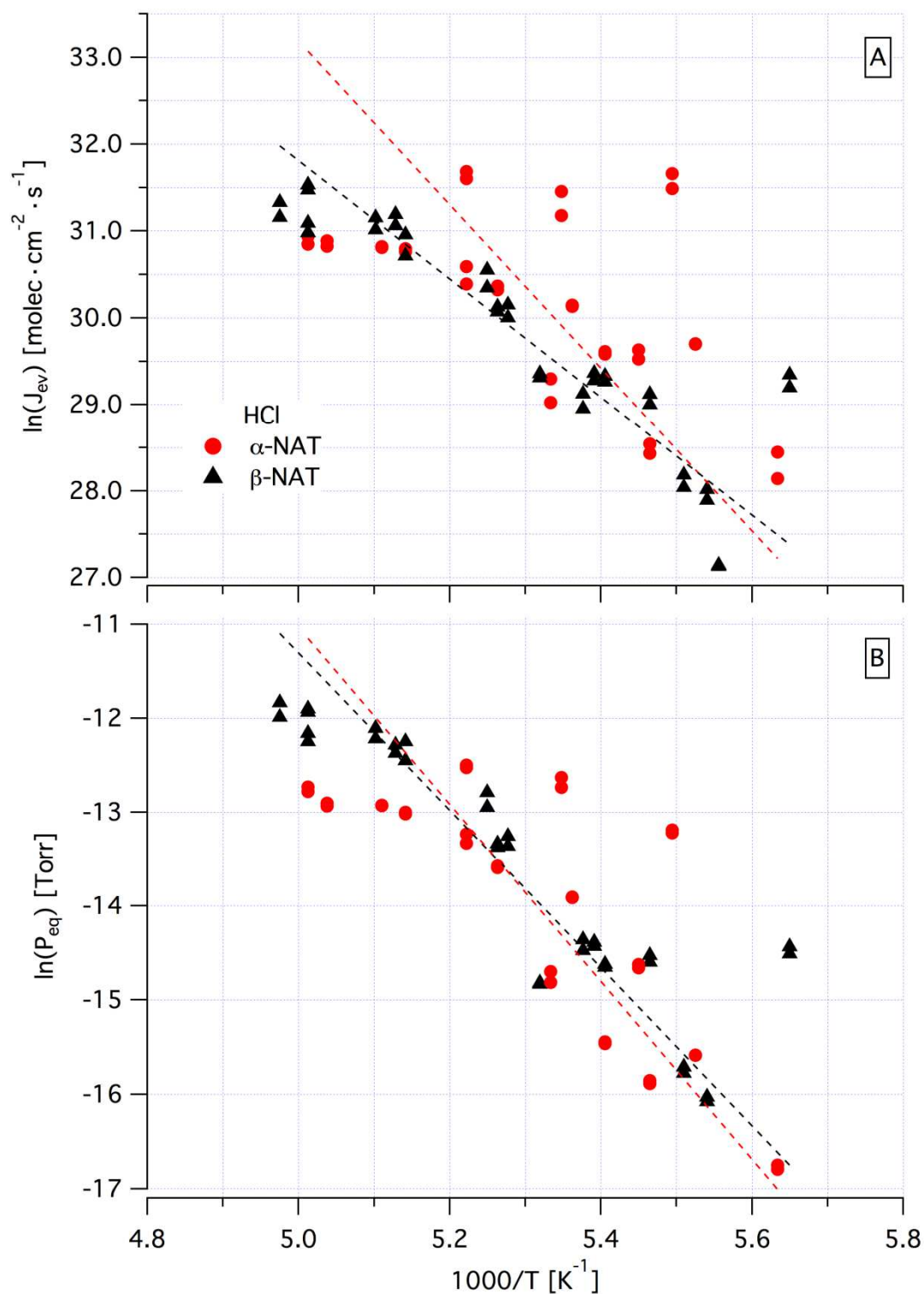
1316

1317 Figure 12: Arrhenius plot of $J_{ev}(\text{H}_2\text{O})$ for β -NAT data displayed in Figure 4b. Full and empty
 1318 red squares represent results of PV and TO experiments, respectively. The equations for the
 1319 linear fits may be found in the text.



1320

1321 Figure 13: Arrhenius plot of $J_{ev}(\text{HNO}_3)$ (A) and van 't Hoff plot of $P_{eq}(\text{HNO}_3)$ (B) for α -NAT
 1322 (Figure 2b and Figure 2c) and β -NAT (Figure 4b and Figure 4c) resulting from TO
 1323 experiments. Full black circles and empty black squares represent the interaction of HNO_3
 1324 with α - and β -NAT films, respectively. The equations for the fitting lines may be found in the
 1325 text.



1326

1327 Figure 14: Arrhenius plot of $J_{ev}(\text{HCl})$ (A) and van 't Hoff plot of $P_{eq}(\text{HCl})$ (B) for α -NAT
 1328 (Figure 8b and Figure 8c) and β -NAT (Figure 9b and Figure 9c) resulting from PV
 1329 experiments. Full red circles and black triangles represent the interaction of HCl with α - and
 1330 β -NAT films, respectively. The equations for the fitting lines may be found in the text.